

# Identification of bipotent progenitors that give rise to myogenic and connective tissues in mouse

Alexandre Grimaldi<sup>1,2,3</sup>, Glenda Comai<sup>1,2</sup>, Sebastien Mella<sup>4,5</sup>,  
Shahragim Tajbakhsh<sup>1,2\*</sup>

<sup>1</sup>Stem Cells and Development Unit, Institut Pasteur, Paris, France; <sup>2</sup>UMR CNRS 3738, Institut Pasteur, Paris, France; <sup>3</sup>Sorbonne Universités, Complexité du Vivant, F-75005, Paris, France; <sup>4</sup>Cytometry and Biomarkers UTechS, Institut Pasteur, Paris, France; <sup>5</sup>Bioinformatics and Biostatistics Hub, Institut Pasteur, Paris, France

**Abstract** How distinct cell fates are manifested by direct lineage ancestry from bipotent progenitors, or by specification of individual cell types is a key question for understanding the emergence of tissues. The interplay between skeletal muscle progenitors and associated connective tissue cells provides a model for examining how muscle functional units are established. Most craniofacial structures originate from the vertebrate-specific neural crest cells except in the dorsal portion of the head, where they arise from cranial mesoderm. Here, using multiple lineage-tracing strategies combined with single cell RNAseq and in situ analyses, we identify bipotent progenitors expressing *Myf5* (an upstream regulator of myogenic fate) that give rise to both muscle and juxtaposed connective tissue. Following this bifurcation, muscle and connective tissue cells retain complementary signalling features and maintain spatial proximity. Disrupting myogenic identity shifts muscle progenitors to a connective tissue fate. The emergence of *Myf5*-derived connective tissue is associated with the activity of several transcription factors, including *Foxp2*. Interestingly, this unexpected bifurcation in cell fate was not observed in craniofacial regions that are colonised by neural crest cells. Therefore, we propose that an ancestral bi-fated program gives rise to muscle and connective tissue cells in skeletal muscles that are deprived of neural crest cells.

\*For correspondence:  
shahragim.tajbakhsh@pasteur.fr

Competing interest: See page 24

Funding: See page 24

Received: 11 May 2021

Preprinted: 26 May 2021

Accepted: 25 February 2022

Published: 28 February 2022

Reviewing Editor: Marianne E Bronner, California Institute of Technology, United States

© Copyright Grimaldi et al. This article is distributed under the terms of the [Creative Commons Attribution License](https://creativecommons.org/licenses/by/4.0/), which permits unrestricted use and redistribution provided that the original author and source are credited.

## Editor's evaluation

This study combines sophisticated lineage tracing and single-cell RNAseq analysis to provide insights into cell fate decision in myogenesis and fibrogenesis. The paper will be of interest to a broad audience of developmental biologists, as it provides evidence for a population of novel bipotent cells, which possess a signature of both muscle and connective tissue.

## Introduction

Stromal cells that are associated with skeletal muscles play critical roles in providing structural support and molecular cues (*Biferali et al., 2019; Kardon et al., 2003; Sefton and Kardon, 2019*). The majority of muscle-associated connective tissues in the head is derived from cranial neural crest cells (NCCs), an embryonic cell population that contributes to most of the structural components of the 'new head', a vertebrate innovation (*Le Douarin and Kalcheim, 1999; Gans and Northcutt, 1983; Grenier et al., 2009; Heude et al., 2018; Noden and Trainor, 2005*). Recently, the extent of this contribution was redefined in muscles derived from cranial mesoderm, including extraocular (EOM), laryngeal and pharyngeal muscles (*Comai et al., 2020; Grimaldi et al., 2015; Heude et al., 2018*;

*Kuroda et al., 2021; Noden and Epstein, 2010*). Interestingly, these muscles contain mesenchyme that is mesoderm-derived in their dorso-medial component, whereas the remaining muscle mass is embedded in mesenchyme that is neural crest-derived. It is unclear how the coordinated emergence of myogenic and connective tissues takes place during development, and how they establish long-lasting paracrine communication.

Along the trunk axis, paraxial somitic mesoderm gives rise to skeletal muscles and associated connective tissues (*Burke and Nowicki, 2003*). Upon signals emanating from adjacent tissues, the dermomyotome (dorsal portion of the somite) undergoes an epithelial-to-mesenchymal transition and gives rise to several cell types including all skeletal muscles of the body, vasculature, tendons and bones (*Ben-Yair and Kalcheim, 2008; Christ et al., 2007*). Similarly, cranial mesodermal progenitors give rise to these diverse cell types, yet, its unsegmented nature raises the question of how spatiotemporal control of these cellular identities is established. Moreover, cardiopharyngeal mesoderm, which constitutes the major portion of cranial mesoderm, has cardiovascular potential, which manifests in the embryo as regions of clonally related cardiac and craniofacial skeletal muscles (*Diogo et al., 2015; Swedlund and Lescroart, 2020*). This skeletal muscle/cardiac branchpoint has been the subject of intense investigation in several model organisms including ascidians, avians, and mouse (*Wang et al., 2019*). While cardiopharyngeal mesoderm was shown to give rise to connective tissues in the mammalian pharynx, the extent of its contribution to other craniofacial muscles in general has not been fully addressed (*Adachi et al., 2020*).

Recently, advanced pipelines integrating scRNAseq data and modern algorithms have been instrumental for identifying new lineage relationships during development (*Cao et al., 2019; He et al., 2020; Qiu et al., 2021*). Here, we employed lineage-restricted single-cell transcriptomics using multiple transgenic mouse lines combined with various computational methods, in situ labeling and loss-of-function experiments, and show that bipotent progenitors expressing the muscle determination gene *Myf5* give rise to both skeletal muscle and anatomically associated connective tissues. Surprisingly, this property was restricted to muscle masses lacking NCC-derived connective tissues, indicating that cranial mesoderm acts as a source of connective tissues in the absence of neural crest cells.

## Results

### Myogenic and non-myogenic mesodermal populations coexist within distinct head lineages

Somitic (*Pax3*-dependent) and cranial (*Tbx1/Pitx2*-dependent) mesoderm give rise to diverse cell types including those of the musculoskeletal system (*Figure 1A*). We first set out to explore the emergence of skeletal muscles and other associated mesodermal tissue within these programs. To that end, we employed a broad anterior mesoderm lineage-tracing strategy using the *Mesp1<sup>Cre/+</sup>; Rosa26<sup>mTmG/+</sup>* line as it labels cranial-derived mesoderm and the anterior somites (*Heude et al., 2018*). At E10.5, when craniofacial skeletal muscles start to be specified, the upper third (anterior to forelimb) of the embryos was dissected, live GFP<sup>+</sup> cells were isolated by FACS, and processed for scRNAseq analysis (*Figure 1—figure supplement 1A-C*). After removal of doublets and lower quality cells (see Materials and methods), a large portion of the cells obtained by *Mesp1<sup>Cre/+</sup>; Rosa26<sup>mTmG/+</sup>* lineage tracing segregated as individual clusters expressing markers of adipogenic, chondrogenic, sclerotomal, endothelial, and cardiovascular lineages as well as the foregut and primitive lung mesenchyme (*Figure 1B, Figure 1—figure supplement 2A-B*). *Pax3*, *Pitx2*, *Tbx1*, *Myf5*, and *Myod* expression were used to identify clusters containing the cranial myogenic progenitors, annotated as 'Cardiopharyngeal mesoderm' and 'Anterior somite' (*Figure 1B-C, Figure 1—figure supplement 2A*).

After subsetting these clusters ('Cardiopharyngeal mesoderm' and 'Anterior somite'), a few subclusters clearly separated based on their origin and anatomical location (*Figure 1D-E, Figure 1—figure supplement 2C*). Surprisingly, about half of the supposedly myogenic cells exhibited a connective tissue signature, including a strong bias toward *Prrx1*, a marker of lateral plate mesoderm (*Durland et al., 2008*), *Col1a1*, a major extracellular matrix component of connective tissue cells (*De Micheli et al., 2020*), and *Twist1*, a key determinant for the mesenchymal properties of cranial mesoderm (*Bildsoe et al., 2016; Figure 1F*). Furthermore, the expression of *Pdgfra*, a well-defined marker of stromal cells (*Farahani and Xaymardan, 2015*), was robustly anticorrelated with the expression of

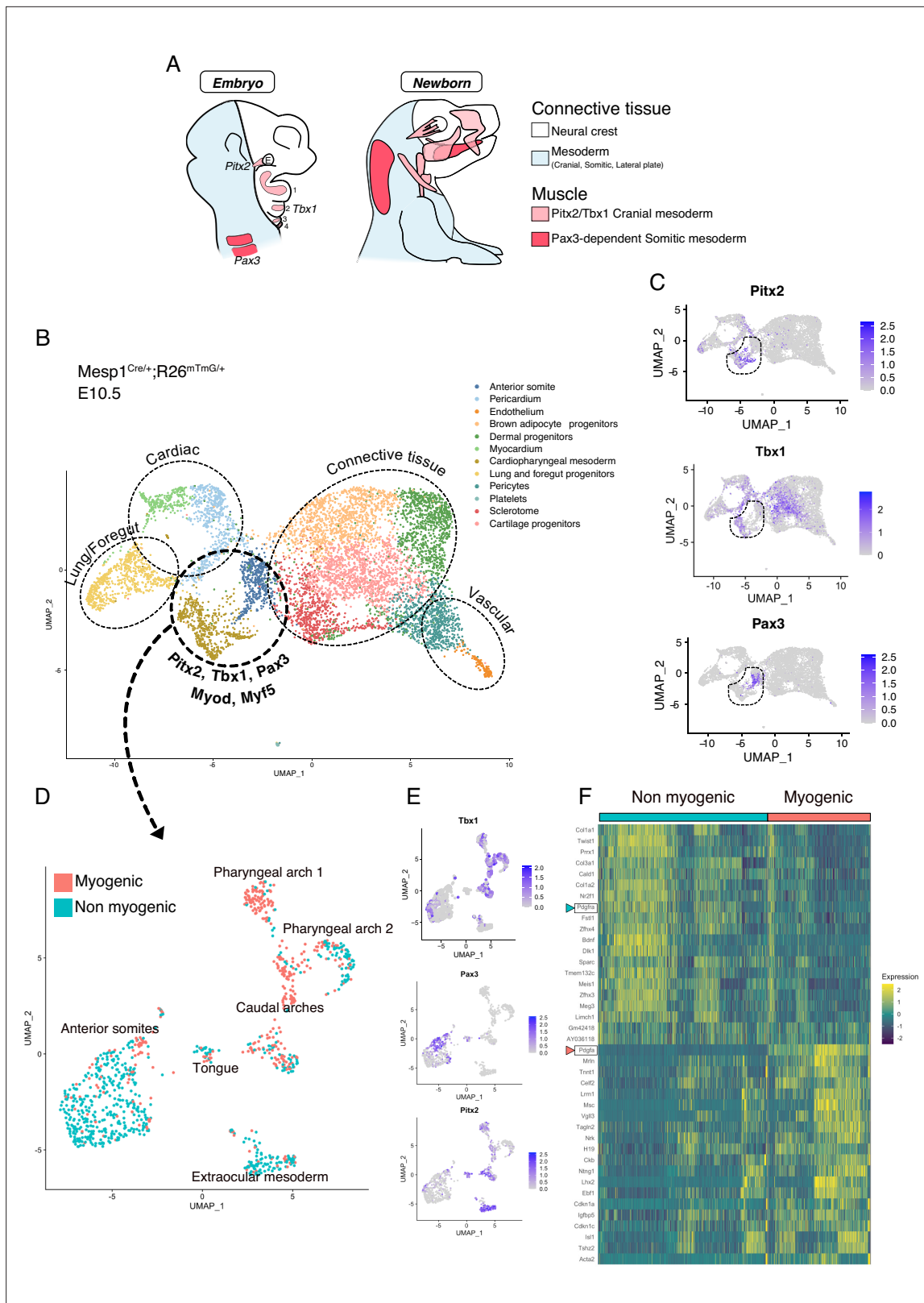


**Figure 1.** scRNAseq reveals non-myogenic populations of cranial mesoderm lineages. **(A)** Scheme of connective tissue origin in the head and known mesodermal upstream regulators. E: Eye, 1–4: Pharyngeal arches 1–4. **(B–F)** scRNAseq analysis on *Mesp1*<sup>Cre/+</sup>; *Rosa26*<sup>mTmG/+</sup> embryos at E10.5 (2 datasets of 2 embryos were aggregated to generate this data, see methods). **(B)** UMAP of *Mesp1*<sup>Cre/+</sup>; *Rosa26*<sup>mTmG/+</sup> E10.5 scRNAseq with main cell types highlighted. The clusters ‘Anterior somite’ and ‘Cardiopharyngeal mesoderm’ were subsetted for further analysis below. **(C)** UMAP expression plots of *Pitx2*, *Tbx1*, and *Pax3*. **(D)** UMAP expression plots of *Myod* and *Myf5*. **(E)** UMAP expression plots of *Tbx1*, *Pax3*, and *Pitx2*. **(F)** Heatmap of gene expression across Non-myogenic and Myogenic populations. *Pdgfra* and *Pdgfra* are highlighted in red and blue, respectively. *Acta2* is highlighted in green. **Figure 1 continued on next page**

Figure 1 continued

*Pitx2* (EOM), *Tbx1* (cranial mesoderm except EOM) and *Pax3* (somitic mesoderm), indicating the clusters of progenitors that were selected. (D) UMAP of progenitor subset annotated as myogenic and non-myogenic based on expression patterns found in E and F. (E) UMAP expression plots of *Pitx2*, *Tbx1* and *Pax3* in the *Mesp1*<sup>Cre/+</sup>; *Rosa26*<sup>mTmG/+</sup> E10.5 subset. (F) Heatmap of top 20 markers of myogenic versus non-myogenic clusters *Mesp1*<sup>Cre/+</sup>; *Rosa26*<sup>mTmG/+</sup> E10.5 subset. *Pdgfra*/*Pdgfa* genes are highlighted.

The online version of this article includes the following figure supplement(s) for figure 1:

**Figure supplement 1.** FACS strategy and preprocessing metrics of the *Mesp1*-derived E10.5 dataset.

**Figure supplement 2.** Genetic markers defining anterior mesodermal tissues.

**Figure supplement 3.** Complementary *Pdgf* signaling defines myogenic and non-myogenic mesodermal cells.

its ligand *Pdgfa* and associated with non-myogenic genes. Conversely, *Pdgfa*, was correlated with a myogenic cell state (Figure 1F, Figure 1—figure supplement 3A-B). Of note, myogenic *Pdgfa* expression was shown to promote adjacent sclerotomal cells to adopt a rib cartilage fate (Tallquist et al., 2000). Therefore, this analysis identified anatomically distinct muscle and closely associated connective tissue progenitors and highlights a potential PDGFR-mediated crosstalk between these 2 cell types.

### Transcriptional trajectories reveal a myogenic to non-myogenic cell state transition

To understand the lineage relationship between myogenic and non-myogenic cells, we exploited the unspliced and spliced variants of our scRNAseq data, and computed the RNA velocity in each cell, using a recently described tool (Bergen et al., 2020; Figure 2, Figure 2—figure supplement 1). RNA velocity interrogates the relative abundance of unspliced and spliced gene variants, which depends on the rates of transcription, degradation, and splicing to infer directional trajectories (Bergen et al., 2020; La Manno et al., 2018). The cell cycle status constitutes a potential bias in scRNAseq data, especially when heterogeneous populations undergo cellular expansion, commitment and differentiation (McDavid et al., 2016). To eliminate this potential bias, cell cycle genes were consistently regressed out during preprocessing and directional trajectories were overlaid with cell cycle phase visualization for comparisons (Figure 2—figure supplement 1A, Materials and methods). Notably, RNA velocity-inferred trajectories suggested that *Myf5*<sup>+</sup> cells from the myogenic compartment contributed to non-myogenic cells (Figure 2A). These calculations were based on gene- and cluster-specific dynamics, which yield higher accuracy than the initially described RNA velocity method, while providing quantitative metrics for quality control (Figure 2—figure supplement 1B-D and Materials and methods).

Another powerful feature of this method is the ability to infer ‘driver genes’ that are responsible for most of the calculated RNA velocity, hence actively transcribed, or repressed (Bergen et al., 2020). Therefore, these genes can identify transitory states underlying cell fate decisions. We used this approach to uncover the driver genes that were responsible for the velocity found in anterior somites, as these cells displayed the most consistent directionality, and appeared to be independent of cell cycle (Figure 2B, Figure 2—figure supplement 1A, Table 1). Top transcribed driver genes included *Foxp1* (Shao and Wei, 2018), *Meox2* (Noizet et al., 2016), *Meis1* (López-Delgado et al., 2020), *Twist2* (Franco et al., 2009), *Fap* (Puré and Blomberg, 2018), *Pdgfra* (Tallquist et al., 2000), *Prrx1* (Leavitt et al., 2020), and *Pcolce* (Bildsoe et al., 2016; Figure 2C), which are associated with fibrosis and connective tissue development. Interestingly, we noted that *Pdgfra* appeared as a driver gene and was activated along this inferred trajectory, whereas *Pdgfa* expression decreased rapidly (Figure 2D). Taken together, RNA velocity analysis for anterior somite mesodermal progenitors showed that *Myf5*<sup>+</sup>/*Pdgfa*<sup>+</sup> cells shifted toward a non-myogenic fate, which includes the down-regulation of *Myf5* and *Pdgfa* and the activation of *Pdgfra* expression (Figure 2E).

### *Myf5*-derived lineage contributes to connective tissue cells in the absence of neural crest

Given that the number of cells examined in the EOM and pharyngeal arch mesodermal clusters from the E10.5 dataset was lower than for anterior somites, we decided to validate the relevance of *Myf5*-derived non-myogenic cells in these cranial regions directly in vivo. We thus examined the EOM, larynx





Figure 2 continued

*Foxp1*, *Meox2*, *Meis1*, *Twist2*, *Fap*, *Pdgfra*, *Prrx1*, and *Pcolce*. Y-axis represents the amount of unspliced transcript per cell; X-axis represents the number of spliced transcripts per cell. A high fraction of unspliced variants indicates an active transcription of the locus, while the inverse indicates inactive/repressed transcription. Dynamics of transcription were inferred at a gene- and cluster-specific level (see Methods). (D) Phase portraits, RNA velocity and expression plots of *Pdgfa* and *Pdgfra* showing splicing dynamics of these two genes. (E) Working model of myogenic and non-myogenic fate decisions from a common bipotent progenitor in anterior somites.

The online version of this article includes the following figure supplement(s) for figure 2:

**Figure supplement 1.** Cell cycle phases and RNA velocity metrics of the *Mesp1*-derived E10.5 dataset.

and upper back muscles in the early fetus at E14.5 using a *Myf5*-lineage reporter mouse (*Myf5*<sup>Cre/+</sup>; *Rosa26*<sup>TdTomato/+</sup>) combined with a contemporary reporter for *Pdgfra* (*Pdgfra*<sup>H2BGFP/+</sup>) (Figure 3). Notably, we observed GFP+ TOM+ double-positive cells in regions of EOM, laryngeal and upper back muscles that are partially or fully deprived of neural crest (Adachi et al., 2020; Comai et al., 2020; Heude et al., 2018; Figure 3A–C). Conversely, no double-positive cells were detected in muscles that are fully embedded in neural crest derived mesenchyme such as mandibular and tongue muscles (Heude et al., 2018; Figure 3D–E).

Mesenchymal tissues associated with the EOM arise from mesoderm in its most dorso-medial portion and from neural crest in its ventro-lateral portion (Comai et al., 2020; Kuroda et al., 2021). This dual origin makes it a prime candidate to explore the relative contribution of *Myf5*-derived cells to the associated connective tissues within a single functional unit. Using *Wnt1*<sup>Cre/+</sup>; *Rosa26*<sup>mTmG/+</sup>; *Myf5*<sup>lacZ/+</sup> (NCC tracing with *Wnt1*) and *Mesp1*<sup>Cre/+</sup>; *Rosa26*<sup>mTmG/+</sup>; *Myf5*<sup>nlacZ/+</sup> (mesoderm tracing with *Mesp1*) at E13.5, we found that GFP+ cells that expressed *Myf5* (β-gal+) were exclusively present in *Mesp1*-derived domains and absent from the *Wnt1* lineage (Figure 3F–I). To further evaluate the contribution of *Myf5*-derived cells to connective tissues in either domain, we re-examined the *Myf5*<sup>Cre/+</sup>; *Rosa26*<sup>TdTomato/+</sup>; *Pdgfra*<sup>H2BGFP/+</sup> mouse line and quantified the percentage of GFP+ TOM+ cells in the EOM. As expected, we observed a medio-lateral gradient of *Myf5*-lineage contribution to EOM-associated connective tissues by E14.5, and this was anticorrelated with the local contribution of neural crest cells to connective tissues (Figure 3J–K). Thus, in agreement with our scRNAseq velocity analysis, these observations suggest that the mesodermal *Myf5*-lineage contributes to muscle-associated connective tissue in domains that are deprived of neural crest mesenchyme.

## Myf5-derived cells can maintain a molecular crosstalk following bifurcation into myogenic and connective tissue fates

To identify the transition between these two fates, we generated an additional scRNAseq dataset based on *Myf5*-lineage tracing at E11.5 (*Myf5*<sup>Cre/+</sup>; *Rosa26*<sup>mTmG/+</sup>) and produced RNA velocity streams (Figure 4A, Figure 4—figure supplement 1). We focused on the EOM and anterior somites, which were clearly distinguished as independent clusters based on the expression of *Alx4* (Bothe and Dietrich, 2006) and *Pax3* (Heude et al., 2018), respectively (Figure 4B). In agreement with the E10.5 mesodermal (*Mesp1*) scRNAseq dataset, these progenitors presented a strong dichotomy in *Pdgfa* and *Pdgfra* expression between myogenic and non-myogenic cells, respectively (Figure 4—figure supplement 1D). Moreover, RNA velocity suggested more myogenic to non-myogenic conversion (Figure 4A, Figure 4—figure supplement 1E–H). To explore further the cell fate transition in these regions, we used a recently described approach by creating a ‘Coexpression score’ based on myogenic and non-myogenic signatures (Kameneva et al., 2021) (see Materials and methods, Figure 4C). This analysis revealed that individual cells undergo a progressive switch from myogenic to non-myogenic gene expression along the inferred trajectories, where cells at the transition zone shut off the myogenic program and start activating fibrogenic genes (Figure 4C heatmap).

To investigate in more detail potential paracrine cell-cell communication between myogenic and non-myogenic cells, we examined their expression patterns within the EOM, given its well-defined morphology (Comai et al., 2020), and its strong myogenic/non-myogenic bi-directional cell-fate (Figure 4D). We performed single molecule fluorescent in situ hybridization (RNAscope) for *Pdgfa* and *Pdgfra* on E14.5 lineage-traced *Myf5*<sup>Cre/+</sup>; *Rosa26*<sup>mTmG/+</sup> fetuses (Figure 4E). In accordance with the scRNAseq analysis, we observed cells exhibiting a mostly non-overlapping, complementary pattern of *Pdgfa* and *Pdgfra* transcripts within the *Myf5*-derived lineage, while retaining anatomical proximity, even at later stages of EOM development.

**Table 1.** Driver genes underlying cell fate decisions in each dataset.

<b>E10.5 Anterior somites</b>	<b>E11.5 EOM Myogenic</b>	<b>E11.5 EOM Non-myogenic</b>	<b>E12.5 Non-myogenic</b>	<b>E14.5 Non-myogenic</b>
Tshz2	Ccdc141	Zfpm2	Mgat4c	Dnm1
Eya1	Mcm6	Plxna4	Cenpv	Pid1
C1qtnf3	Dync1i1	Col23a1	C130073E24Rik	Nrp2
Meis2	Tpm2	Edil3	Tbx3os1	Ntrk3
Limch1	Celf2	Map2	E330013P04Rik	Tmem132c
Moxd1	Sox6	Rora	Stk26	Egflam
Epha4	Tnc	Sema5a	Edil3	Gpr153
Pitx2	Magi3	Colec12	Fdft1	Efemp1
Parm1	Sh3glb1	Smoc1	Lima1	Adamts2
Hpse2	Parm1	Ptptrt	Trim59	Brinp1
Lrrn1	Ephb1	Ror1	Meg3	Vegfc
Dmrt2	Bmpr1b	Dock5	Gins3	Twist2
Myl3	Hells	Map1b	Tpm2	Itgb5
Fap	Pdgfc	Fn1	Cdh6	Gria1
Hs6st2	Ptprd	Limch1	Csmd3	Sned1
Ddr2	Cnr1	Tenm4	Tceal5	Sorcs3
Cald1	Sema3d	Rbms3	Pclaf	Ebf2
Prrx1	Clcn5	Srgap3	Tspan9	Fam19a1
Magi3	Chd7	Tmem132c	Eps8	Trabd2b
Ntn1	Col25a1	Sdc2	Lmna	Plxdc2
Zfhx3	Reep1	Add3	Dmrt2	Sh3gl3
Meis1	Ctnnal1	Pdgfra	Cpeb4	Luzp2
Tnni1	Tpm1	Gmns	Hpgd	Pdzd2
Crym	Zim1	St6galnac3	Rcsd1	Sema3e
Ebf1	Lmx1a	Epb4113	Pdgfra	Rims1
Nr2f1	Neb	Pde3a	Plac1	Epha3
Ntng1	Atad2	Tox	Palmd	Cyp7b1
Pgm5	Dapk2	Smarca2	Gucy1a1	Gem
Cdh6	Prox1	Ctdspl	Wif1	Ldb2
Foxp1	Lsamp	Magi2	Naalad2	Scube1
Celf2	Ttn	Dpysl3	Smoc2	Pdgfra
Tbx1	Pls3	Fgfr2	Rassf4	Pde1a
Bdnf	Slf2	Ldb2	Pttg1	Nde1
Colec12	Vat1l	Igf1	Josd2	Enpp2
Eya4	E2f1	Elk3	Plxna4	Fam107b
Sobp	Epb4112	Zmiz1	Eya2	Stxbp6
Peg3	Gm28653	Dlc1	Nrsn1	Rerg
Pdgfra	Lrrn1	Nhs	Fign	Prex2
Nrk	Mef2c	Cdkn1c	Inpp1	Man1a
Ptn	St8sia2	Plpp3	Rnf152	Tmem45a

Table 1 continued on next page

Table 1 continued

<b>E10.5 Anterior somites</b>	<b>E11.5 EOM Myogenic</b>	<b>E11.5 EOM Non-myogenic</b>	<b>E12.5 Non-myogenic</b>	<b>E14.5 Non-myogenic</b>
Daam1	Tshz1	Ebf1	Lasp1	Sh3bp4
Dlk1	Wee1	Sorbs2	Mrln	Mcc
Unc5c	Slc24a3	Baz1a	Cdt1	Ncald
Lpar1	Ncoa1	Fat4	Notch3	Kdelr2
Syne2	Dek	Golgb1	Pax3	Pcdh19
Nkd2	Kdm5b	Hpse2	Egfr	Gas7
Brinp1	Unc13c	Samd4	Dbf4	Cpt1c
Zfhx4	Ddr1	Itga9	Bcr	Adam22
Nnat	Pip4k2a	Magi1	Mllt3	Itgb8
Gxylt2	Fndc3c1	Pcdh9	Nectin1	Dchs2
Clmp	Rbm24	Tgfb2	Grin3a	Cep350
Ror2	Rreb1	Ntf3	Cbfa2t3	Oat
Nfia	Rragd	Col11a1	Cdh2	Rab30
Ebf2	Acsl3	Runx1t1	Anln	Aff2
Ednra	Acvr2a	Tnrc18	Ccdc6	Gna14
Fli1	Zeb1	Crym	Mcu	Slc29a1
Tspan12	Rgma	Fap	Fnip2	Pls3
Ttc28	Arpp21	Ppp1r1a	Kcnk13	Traf3ip1
Nfib	Lef1	Tes	Sned1	Rcsd1
Ccdc88c	Nr2f2	Bicc1	Nde1	Lgr4
Col13a1	Foxo1	Il1rap1	Hipk3	Zfp9
2700069I18Rik	Pdzrn4	Alcam	Arhgap11a	Hs3st5
Pcolce	Hmga2	2700069I18Rik	Fam8a1	Aspn
Scn3a	Lurap1l	Dab2	Kif21a	Nrxn1
Acvr2a	Pkig	Cntln	Mtss1	Rrm1
Auts2	Ncl	Clmn	Abcd2	Igfbp7
Col3a1	CT025619.1	Rbms1	Irx5	Slc35f3
Gap43	Erbp4	Tmem2	Pacs2	Kif15
Mrln	Cdk14	Cdh6	Nab1	Slc1a3
Pax3	Kif21a	Lypd6	Ccnd2	Bmp6
Sim1	Zfp704	Mmp2	Bok	Dkk2
Epb41l2	Nasp	Kif5c	Dok5	Tspan9
Ppp3ca	Plekha5	Cadm2	Ncapg	Ets1
Tnfaip6	Cap2	Prkg2	Rfx8	Gria3
Tmem132c	Snca	Cped1	Fhod3	Sox8
Tmem2	Epha4	Dtl	Tk1	Melk
Epb41l3	Atad5	Ror2	Asf1b	Ntm
Crybg3	Cntn3	Utrn	Tek	Synpo2l
Nrxn1	Cacna2d1	Foxp1	Arfgef3	Hlf
Farp1	Pak3	L3mbtl3	Rnf182	Adamts5

Table 1 continued on next page

Table 1 continued

E10.5 Anterior somites	E11.5 EOM Myogenic	E11.5 EOM Non-myogenic	E12.5 Non-myogenic	E14.5 Non-myogenic
Sulf1	Megf10	Cdh23	Kif14	Plcb4
Tmtc2	Tnnt1	Negr1	1810041L15Rik	Cdc25b
Pde4dip	Acta2	Hmcn1	Rrm2	Mgat4a
Phldb2	Barx2	Col26a1	Fgf5	Mdfic
Plpp3	Mrln	Fbn2	Barx2	Trpc5
Ybx3	Pgm5	Ankrd12	Fli1	Kif4
Ppm1l	Fmr1	Lhfp	Jph2	Plce1
Twist2	Smc4	Hs3st3b1	Dtx4	Il17rd
Nuak1	Clmp	Adgrl3	Ncald	Mmp16
Tgfb2	Alpk2	Svil	Zic4	Hhip
Sfrp1	Kctd1	Mob3b	Dlc1	Tpx2
Sncaip	Meg3	Trabd2b	Cdc45	Ndc80
Tenm3	Samd5	Rmst	Gatm	Bub1b
Cdh2	Nrk	Prrx1	Ssc5d	Hmmr
Iqgap2	Piezo2	5330434G04Rik	Phactr2	Kank4
App	Robo1	Zfhx3	Ppp1r14c	Tmeff2
Pgam2	Col1a2	Foxp2	Agl	Nr4a1
Rspo3	Cntrl	Mpp6	Tox3	Aurkb
Cdon	Mllt3	Crispld1	Aurka	Lrrtm3
Ebf3	Peg3	Eya1	Cdh15	Cenpq

Gene set enrichment analysis of EOM myogenic and non-myogenic driver genes showed that transmembrane receptor protein kinase and SMAD activity were shared terms between the two clusters, suggesting that specific complementary signaling networks could be actively maintained between these two populations (**Figure 4—figure supplement 2A**). Both signaling pathways were reported to act as inhibitors of myogenic differentiation and could therefore be associated with progenitor cell maintenance (**Arnold et al., 2020; Cossu et al., 2000**). Notably, *Bmpr1b* and *Ephb1* were among the top 100 driver genes of the myogenic EOM compartment, suggesting that myogenic commitment is associated with upregulation of these kinase receptors in the EOM (**Figure 4—figure supplement 2B, Table 1**). Strikingly, two of their respective ligands, *Bmp4* and *Efnb1*, were preferentially expressed in non-myogenic cells. Analysis of their expression patterns in E14.5 embryos by RNAscope validated these complementary expression patterns in adjacent muscle and connective tissue domains (**Figure 4F–H**). These results favor a model where paracrine signaling networks operate between myogenic and non-myogenic *Myf5*-derived cells (**Figure 4I**), while their cellular juxtaposition is maintained through fetal stages.

### Obstructing myogenesis expands connective tissue formation from bipotent cells

The directional trajectories identified by RNA velocity in the EOM at E11.5 showed a strong bidirectionality in fate with a higher velocity confidence index at each end of the myogenic and non-myogenic domains, and lower at their interface (**Figure 5—figure supplement 1A**). This suggested that cells at the interface are bipotent while cells located on either side of this central region are committed either to a myogenic-or non-myogenic fate. To identify the regulatory factors underlying this potential bipotency, we used SCENIC, a regulatory network inference algorithm (**Aibar et al., 2017**). This tool allows regrouping of sets of correlated genes into regulons (each regulon consists of a transcription factor and its targets) based on binding motifs and co-expression. The top regulons of



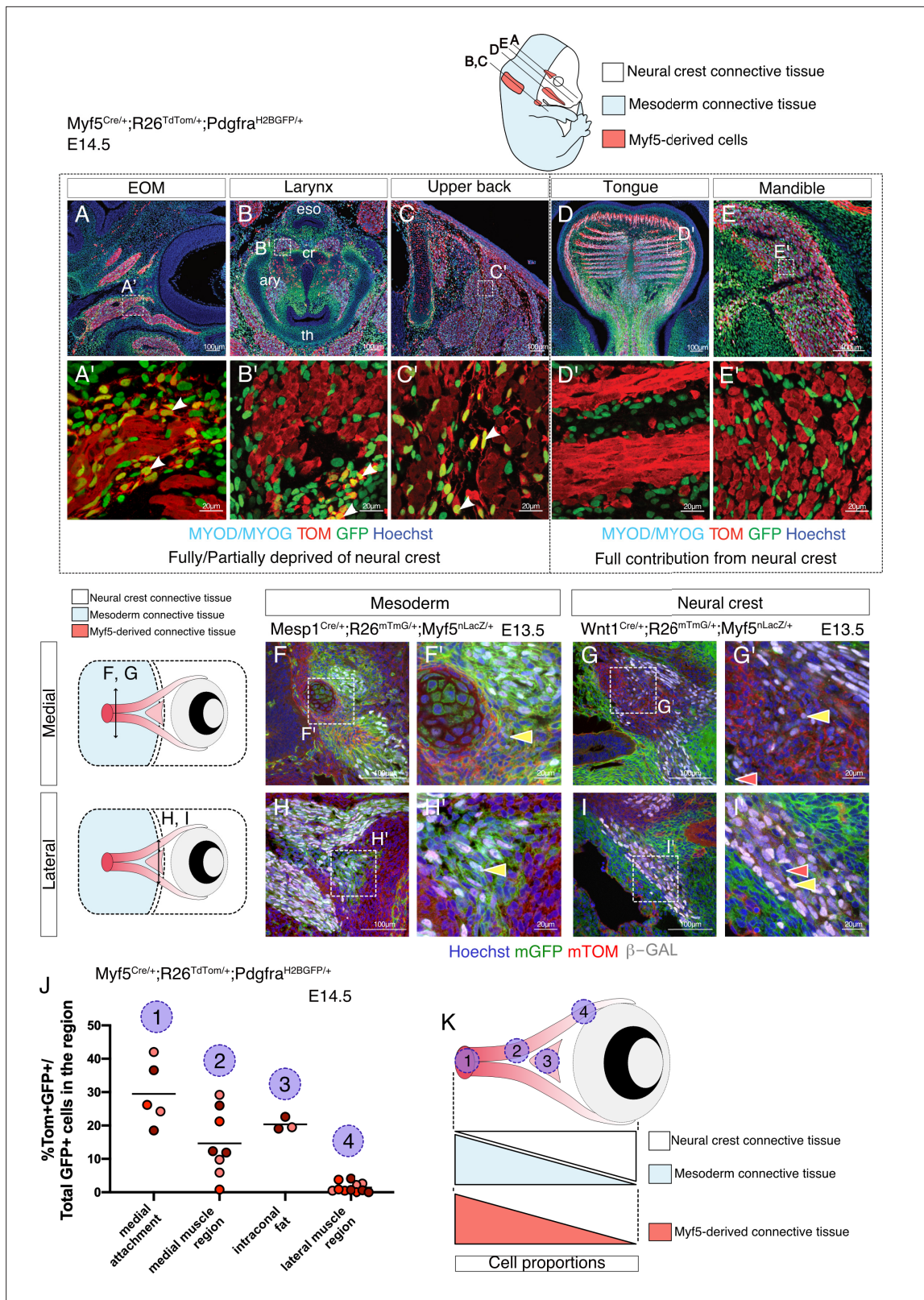


**Figure 3.** Myf5-derived mesodermal connective tissue partially compensates for the lack of neural crest. (A-E') Transverse sections of an E14.5 *Myf5<sup>Cre/+</sup>; Rosa26<sup>TdTomato/+</sup>; Pdgfra<sup>H2BGFP/+</sup>* embryo immunostained for Myod/Myog. White arrowheads indicate cells double-positive GFP/TOM and negative for Myod/Myog (n = 3 embryos). (F-I') Transverse cryosections of the EOM at E13.5 of *Wnt1<sup>Cre/+</sup>; Rosa26<sup>mTmG/+</sup>; Myf5<sup>nLacZ/+</sup>* (G,I) and *Mesp1<sup>Cre/+</sup>; Rosa26<sup>mTmG/+</sup>; Myf5<sup>nLacZ/+</sup>* (F,H) immunostained for β-gal, at the level of the medial attachment (F,G) and lateral muscle masses (H,I). Yellow arrowheads indicate

Figure 3 continued on next page

Figure 3 continued

Myf5-expressing cells in the context of mesodermal and neural crest lineages. Note that Myf5-expressing cells are mGFP<sup>+</sup> in the Mesp1 lineage and mGFP<sup>-</sup> in the Wnt1 lineage. Red arrowheads indicate neural-crest cells that are excluded from the Myf5 lineage (n = 2 embryos for each). (J) Scatter plots of the proportion of double positive cells in E14.5 Myf5<sup>Cre/+</sup>; Rosa26<sup>TdTomato/+</sup>; Pdgfra<sup>H2BGFP/+</sup> embryos in various regions throughout the EOM (the line is the mean, each dot is a tissue section, each color is a different embryo, n = 3 embryos). (K) Scheme highlighting the quantified regions in (J) and summarising the contribution of each population to periocular connective tissues. TOM: TdTOMATO.

The online version of this article includes the following source data for figure 3:

**Source data 1.** Excel table summarizing the quantification displayed on **Figure 3J**.

this analysis revealed active transcription factors underlying myogenic and non-myogenic cell fates in the EOM at E11.5. Notably, *Myf5*, *Pitx1*, *Mef2a*, and *Six1*, transcription factors known to be implicated in myogenic development (Buckingham and Rigby, 2014), appeared among the top regulons in myogenic cells whereas *Fli1*, *Ebf1*, *Ets1*, *Foxc1*, *Meis1*, and *Six2*, genes known for their involvement in adipogenic, vascular, mesenchymal and tendon development (Jimenez et al., 2007; López-Delgado et al., 2020; Noizet et al., 2016; Truong and Ben-David, 2000; Whitesell et al., 2019; Yamamoto-Shiraishi and Kuroiwa, 2013), constituted some of the highly active non-myogenic transcription factors (Figure 5A). Interestingly, recent work uncovered *Fli1* as a potential regulator of vascular fate in multipotent myogenic progenitors (Ferdous et al., 2021). Accordingly, we found that *Scube1*, a gene known for its involvement in vasculature development, was upregulated in the Pdgfra<sup>+</sup> non-myogenic fraction of the EOM (Figure 5—figure supplement 1B). RNAscope in situ hybridization confirmed these findings and showed that *Scube1* was expressed at the level of the EOM medial attachment at E14.5 (Figure 5—figure supplement 1C-E). In addition, *Scube1* was reported to promote BMP signaling (Liao et al., 2016). Thus, the EOM tendon attachment seems to rely on transcription factors and markers that are typically vascular, hence suggesting that some of them are coopted.

Given that *Myf5* appeared itself as a top myogenic regulon (Figure 5A), we interrogated the fate of *Myf5*-expressing progenitors in a *Myf5*<sup>nlaZ/nlaZ</sup> null embryos at E12.5 (Figure 5B-E). As previously reported, the EOMs are absent in this mutant (Figure 5C, asterisk) (Sambasivan et al., 2009). Interestingly, some β-gal<sup>+</sup> cells were found in the cartilage primordium (Sox9<sup>+</sup>) of the EOM in the heterozygous control indicating that cells with recent *Myf5* activity diverged to this non-myogenic fate (Figure 5D-D'). Notably, disruption of *Myf5* activity led to a threefold increase in the proportion of non-myogenic *Myf5*-derived cells in this region (Figure 5E-F). In contrast, no double-positive cells were found in the masseter, a muscle fully embedded in neural crest-derived connective tissue, even in the absence of *Myf5* (Figure 5F). *Myf5* expression is thus necessary to maintain a balance between myogenic and non-myogenic cell fates of *Myf5*<sup>+</sup> progenitors only in neural crest-depleted regions. In contrast, very few Pdgfra<sup>+</sup> cells were found to be derived from *Myod* expressing cells in *Myod*<sup>iCre</sup>; Rosa26<sup>TdTomato/+</sup>; Pdgfra<sup>H2BGFP/+</sup> fetuses at E14.5, particularly in the EOM and the back muscles (about 3 and 1.5 cells per 100 μm<sup>2</sup> of muscle, respectively) (Figure 5G, I, J). Accordingly, the masseter lacked *Myod*-derived connective tissue cells (Figure 5H and J). These observations indicate that progenitors that bifurcate to myogenic and non-myogenic cell fates are present only in neural-crest depleted regions. This property is associated primarily with *Myf5* expression, as subsequent activation of *Myod* within this lineage appears to lock cell fate into the myogenic program and suppress their connective tissue potential (Figure 5K).

### Myf5-derived connective tissues are observed in fetal stages

Although we identified *Myf5*-derived non-myogenic cells in various regions of the embryo, it was not clear if this population was continuously generated throughout development. To address this issue, we performed two more scRNAseq experiments at E12.5 and E14.5, using contemporary *Myf5* labeling, which led to much fewer non-myogenic cells that could be captured (*Myf5*<sup>GFP-P/+</sup>; Figure 6, Figure 6—figure supplement 1, Figure 6—figure supplement 2). In accordance with the earlier datasets, some cells that appeared to belong to muscle anlagen of EOM, somites and caudal arches progressed toward a non-myogenic state (Figure 6A-C'). To assess the identity of these cells, we performed a gene set enrichment network analysis combining the differentially expressed genes of non-myogenic clusters of all stages. We found that all stages contributed relatively equally to each 'GO Molecular Function' and 'Reactome pathways' terms despite their relatively diverse gene expression signatures (Figure 6D-E', Figure 6—figure supplement 3). This suggests that these non-myogenic cells are

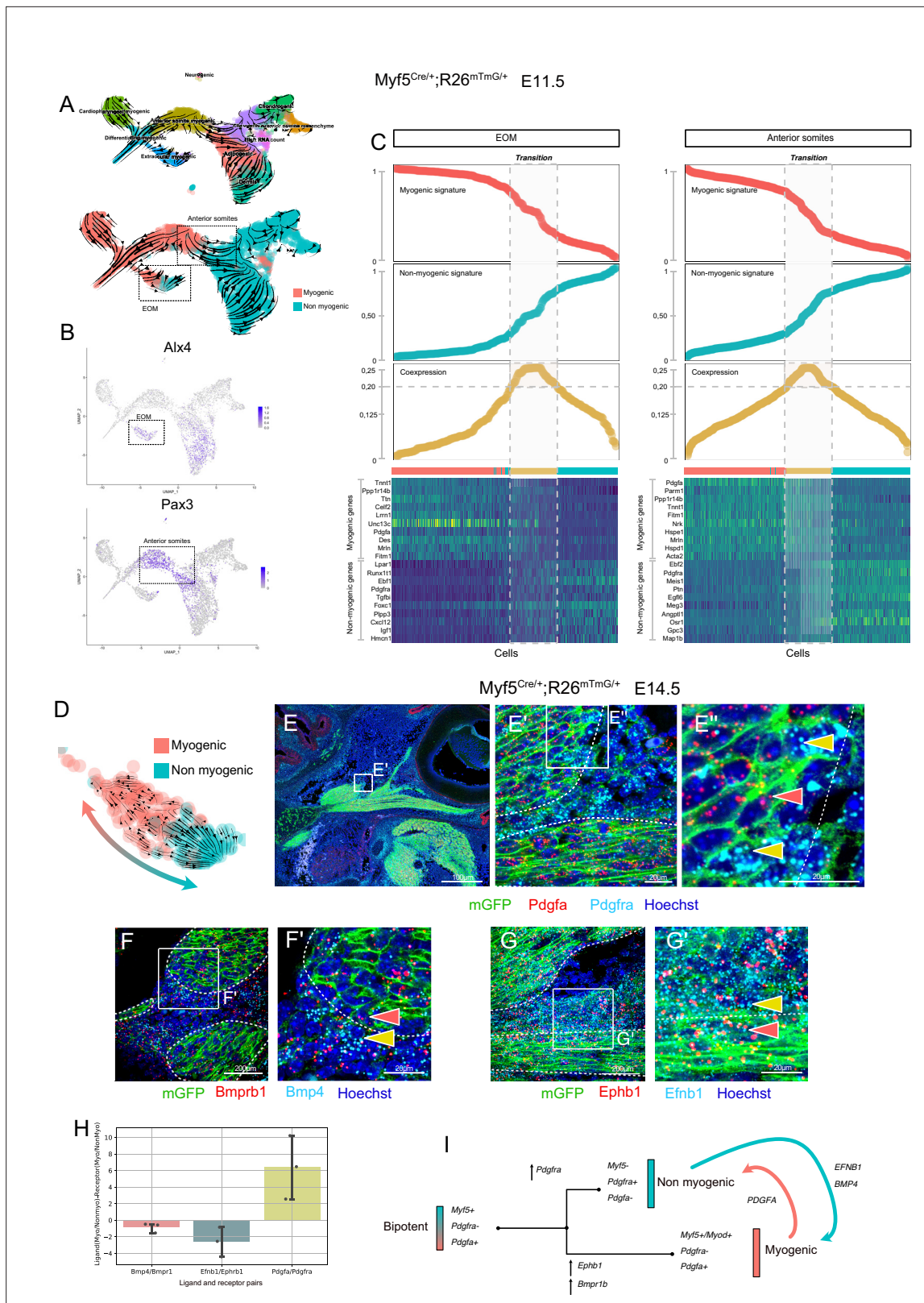


**Figure 4.** Maintenance of signaling cues between *Myf5*-derived myogenic and non-myogenic cells in EOM. **(A–D)** scRNAseq analysis of the *Myf5<sup>Cre/+</sup>; Rosa26<sup>mTmG/+</sup>* E11.5 dataset (2 datasets of 2 embryos were aggregated to generate this data, see Materials and methods). **(A)** UMAPs of *Myf5<sup>Cre/+</sup>; Rosa26<sup>mTmG/+</sup>* E11.5 RNA velocity trajectories. **(B)** Expression plots of *Alx4* and *Pax3*, highlighting EOM and Anterior somite clusters, respectively. **(C)** Plots of Myogenic and Non-myogenic signatures, Coexpression score and heatmaps of top markers, highlighting the transition population in EOM and

Figure 4 continued on next page



Figure 4 continued

anterior somites. Cells are ordered based on their non-myogenic signature score (increasing). The coexpression score is the product of the myogenic and non-myogenic signatures. Cells presenting a coexpression score higher than 0.20 are highlighted in yellow. These cells represent the transition between the myogenic and non-myogenic fates. (D) UMAP of the EOM subset revealing the bipartite fate of *Myf5*-expressing cells. (E-G') RNAscope on *Myf5<sup>Cre/+</sup>; Rosa26<sup>mTmG/+</sup>* E14.5 tissue sections with *Pdgfra* (cyan) and *Pdgfa* (red) probes (E-E'), *Bmprb1* (red) and *Bmp4* (cyan) probes (F-F') and *Ephb1* (red) and *Efnb1* (cyan) probes (G-G'). *Myf5*-derived cells are labelled by membrane GFP staining (n = 3 embryos each). Red and yellow arrowheads indicate *Myf5*-derived myogenic and non-myogenic cells respectively. The dotted lines highlight the boundary of the muscle masses. (H) Quantification of the Ligand-Receptor scores for each pair (see Materials and methods). Note that these ratios are negative in the case of Bmp and Eph (signaling from non-myogenic to myogenic) but positive for Pdgf (signaling from myogenic to non-myogenic). (G) Model of myogenic and non-myogenic cell communication following bifurcation from a bipotent cell.

The online version of this article includes the following source data and figure supplement(s) for figure 4:

**Source data 1.** Excel table summarizing the quantification displayed on **Figure 4H**.

**Figure supplement 1.** FACS strategy, preprocessing metrics, expression patterns, and RNA velocity metrics of the *Myf5*-derived E11.5 dataset.

**Figure supplement 2.** Kinase signaling complementarity in the EOM at E11.5.

relatively homogeneous in gene signatures throughout cranial muscles. Highly significant terms hinted at a myogenic-supporting role, providing muscle progenitors with extracellular matrix components, and contributing to neuronal guidance (**Figure 6E**). Among these terms, presence of Pdgf signalling and receptor kinase activity indicated, once again, that the interactions found in the EOM could occur also at later stages in various craniofacial muscles that are deprived of neural crest derived connective tissue.

### A novel regulatory network underlies the non-myogenic cell fate

*Myf5*<sup>+</sup> bipotent progenitors were observed at multiple stages and anatomical locations, and they yielded a relatively homogeneous population expressing common markers associated with extracellular matrix components, cell adhesion molecules, and kinase signalling. To assess whether the regulatory mechanisms guiding this transition are distinct in different locations in the head, we set out to explore the common molecular switches underlying cell fate decisions. To do so, we developed a pipeline where we combined the list of driver genes at the start of the non-myogenic trajectory (**Table 1**) with the most active regulons in the non-myogenic region (Materials and methods, code in open access). This resulted in a network consisting of the most active transcription factors and the most transcriptionally dynamic genes found at the non-myogenic branchpoint. We performed this operation for each dataset independently and displayed them as individual networks (**Figure 7—figure supplement 1A-D**). Finally, we overlapped the list of these 'driver regulators' to identify the common transcription factors guiding the non-myogenic cell fate decision (**Figure 7A**). Notably, *Foxp2*, *Hmga2*, *Meis1*, *Meox2*, and *Tcf7l2* were identified in all four scRNAseq datasets as key driver regulators, and thus are likely to play significant role in the non-myogenic transition (**Figure 7A, Table 2**).

Forkhead box transcription factors FOXC1 and FOXC2 were reported to regulate the balance between myogenic and vascular lineages within somites (**Lagha et al., 2009; Mayeuf-Louchart et al., 2016**). Interestingly, *Foxc1* has been reported to promote both cranial vasculature and cranial cartilage development in zebrafish (**Whitesell et al., 2019; Xu et al., 2021**). FOXP2 immunostaining on *Myf5<sup>Cre/+</sup>; Rosa26<sup>TdTom/+</sup>; Pdgfra<sup>H2BGFP/+</sup>* E12.5 embryos showed that the *Myf5*-derived EOM cells expressed a relatively high level of *Foxp2* compared to mandible and trunk muscles, consistent with their apparent high contribution to connective tissue (**Figure 7B-E**).

To gain further insights into the transitioning population, we performed FACS analysis of dissected head, limb and trunk regions of *Myf5<sup>Cre/+</sup>; Rosa26<sup>TdTom/+</sup>; Pdgfra<sup>H2BGFP/+</sup>* embryos at E12.5 (**Figure 7F-G**). We focused on TOM<sup>+</sup> cells (*Myf5*-lineage) and assessed their GFP expression levels as a readout of their commitment toward connective tissue. This analysis identified non-FAPs cells (GFP<sup>low</sup>) transitioning towards a *Pdgfra*<sup>+</sup> state in head and trunk regions but very few in the limb (**Figure 7G**). Interestingly, while trunk muscles presented the largest portion of transitioning cells (40%), a similar transitioning population was noted in the head (20%) despite a large contribution of NCC to head connective tissues. Thus, cardiopharyngeal mesoderm may have a superior potential to give rise to connective tissue compared to somite-derived progenitors in the limb (1.5%).

In addition, Tcfs and Lef1 were among the top common regulators identified, and they form a complex effector for the canonical Wnt pathway. Previous work showed that during cranial myogenesis,

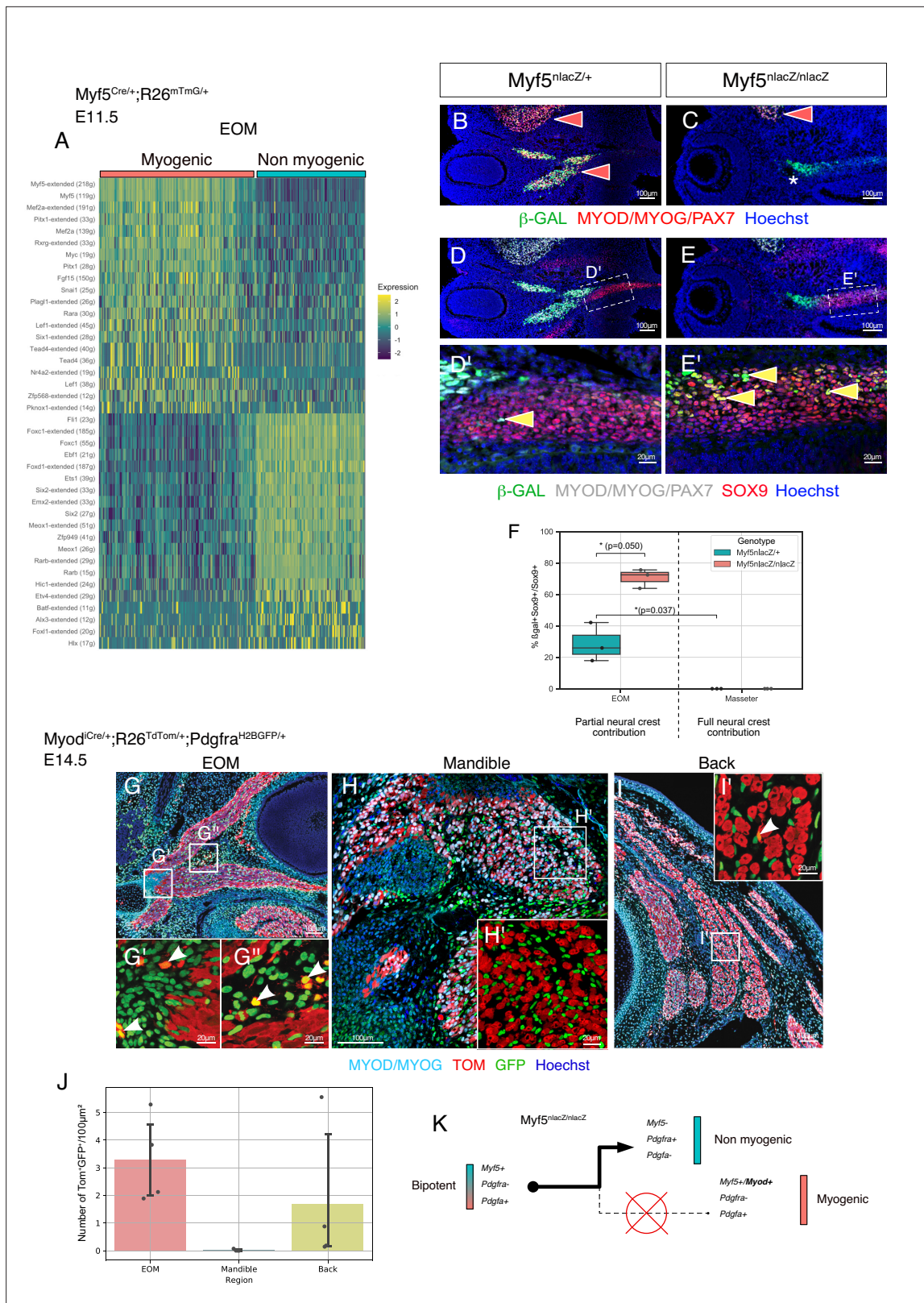


**Figure 5.** Disruption of *Myf5* increases the connective tissue output from bipotent cells. **(A)** Heatmap of top regulons (transcription factor and associated targets) of the EOM subset of the *Myf5<sup>Cre/+</sup>; Rosa26<sup>mTmG/+</sup>* E11.5 dataset. The suffix ‘\_extended’ indicates that the regulon includes motifs that have been linked to the TF by lower confidence annotations, for instance, inferred by motif similarity. Number in brackets indicates number of genes comprising the regulon (n = 2 pooled datasets). **(B–C)** Transverse sections of *Myf5<sup>nlacZ/+</sup>* **(B)**, and *Myf5<sup>nlacZ/nlacZ</sup>* **(C)** embryos in the EOM region at E12.5

Figure 5 continued on next page



Figure 5 continued

immunostained for  $\beta$ -gal (green), and Myod/Myog/Pax7 (red). Red arrowheads indicate  $\beta$ -gal/ Myod/Myog/Pax7 double positive cells in control EOM/ Masseter and in mutant Masseter. Asterisk highlights the lack of myogenic progenitors in the EOM region of the mutant embryo, indicated by the absence of Myod/Myog/Pax7 staining. (D-E') Transverse sections of *Myf5<sup>nlacZ/+</sup>* (D-D'), and *Myf5<sup>nlacZ/nlacZ</sup>* (E-E') in the EOM region at E12.5 immunostained for  $\beta$ -gal (green), Sox9 (red), and Myod/Myog/Pax7 (gray). Yellow arrowheads indicate  $\beta$ -gal/Sox9 double positive cells and show an expansion of this cell population in the mutant. (F) Quantification of proportion of  $\beta$ -gal+;Sox9+ double positive cells in the total Sox9+ population of the EOM and Masseter muscles. Each dot is a different sample, the center line of the boxplot is the median value. (n = 3 embryos, p-values were calculated using a two-sided Mann-Whitney U test). (G-I') Transverse sections of *Myod<sup>flCre/+</sup>; Rosa26<sup>TdTomato/+</sup>; Pdgfra<sup>H2BGFP/+</sup>* embryos at E14.5 immunostained for Myod/ Myog (committed and differentiating myoblasts) in the extraocular (G-G'), mandibular (H-H'), and back muscles (I-I'). White arrowhead indicates double positive cells (GFP+ TOM+). (J) Quantification of double positive cells (GFP+ TOM+) in EOM, mandibular muscles and back muscles per 100  $\mu$ m<sup>2</sup> area on *Myod<sup>flCre/+</sup>; Rosa26<sup>TdTomato/+</sup>; Pdgfra<sup>H2BGFP/+</sup>* sections shown in E-G (n = 4 embryos). (K) Model of lineage progression from bipotent cells in a *Myf5* null background.

The online version of this article includes the following source data and figure supplement(s) for figure 5:

**Source data 1.** Excel table summarizing the quantification displayed on **Figure 5F**.

**Source data 2.** Excel table summarizing the quantification displayed on **Figure 5J**.

**Figure supplement 1.** The vascular marker *Scube1* is expressed in *Myf5*-derived non-myogenic cells in the EOM.

**Figure supplement 1—source data 1.** Excel table summarizing the quantification displayed on **Figure 5—figure supplement 1E**.

neural crest cells release inhibitors of the Wnt pathway to promote myogenesis (Tzahor et al., 2003). It is thus tempting to speculate that in the absence of neural crest, mesoderm-derived progenitors can give rise to connective tissue by maintaining canonical Wnt activity. To test this hypothesis, we examined the expression of Axin2, a common readout for Wnt/ $\beta$ -cat activity (Babb et al., 2017; van de Moosdijk et al., 2020). Interestingly, Axin2 levels were elevated in the non-myogenic portion of all the different datasets (Figure 7—figure supplement 1E-H). Additionally, Dkk2, which has been described as an activator of Wnt/ $\beta$ -cat pathway in the neural crest (Devotta et al., 2018), was also found to be elevated, indicative of a putative positive-feedback loop mechanism supporting the maintenance of this population.

## Discussion

Distinct fates can emerge through the specification of individual cell types, or through direct lineage ancestry from bipotent or multipotent cells. Here, we addressed this issue in the context of the emergence of myogenic and associated connective tissue cells during the formation of craniofacial muscles. By combining state-of-the-art computational methods and in-situ analyses, we identified the transcriptional dynamics, the intercellular communication networks, and the regulators controlling the balance between complementary cell fates. Specifically, our work provides evidence for a novel mesoderm-derived bipotent cell population that gives rise to muscle and associated connective tissue cells spatiotemporally, and only in regions deprived of neural crest cells (Figure 7—figure supplement 2).

Brown adipocytes, neurons, pericytes, and rib cartilage have been reported to express *Myf5* in ancestral cells (Daubas et al., 2000; Haldar et al., 2008; Sebo et al., 2018; Stuelsatz et al., 2014). Interestingly, when *Myf5* expression is disrupted, cells can acquire non-myogenic fates and contribute to connective tissue (this study), cartilage, and dermis (Tajbakhsh et al., 1996), while others remain apparently undifferentiated (cells labeled with an asterisk in Figure 5C). It is likely that these cells are undergoing apoptosis as reported previously (Sambasivan et al., 2009). These studies suggest that *Myf5*-expression alone is not sufficient to promote robust myogenic fate in multiple regions of developing embryos. Consistent with these observations, Myod+ cells do not contribute to rib cartilage (Wood et al., 2020) and give rise to few connective tissue cells in the periocular and back regions (this study). These findings are also consistent with the role of *Myod* in defining the committed myogenic cell state and its higher chromatin-remodelling capacity compared to *Myf5* (Conerly et al., 2016; Tapscott, 2005). In contrast to a previous study (Stuelsatz et al., 2014), we found no neural-crest derived cells expressing *Myf5* during EOM tissue genesis at E13.5 (using *Wnt1<sup>Cre/+</sup>; Rosa26<sup>mTmG/+</sup>; Myf5<sup>nlacZ/+</sup>*). We note that *Myf5*-expressing cells contribute to non-myogenic cells from early embryonic stages (E10.5) and continue to do so in the fetus, indicating that these bipotent cells persist well after muscles are established.

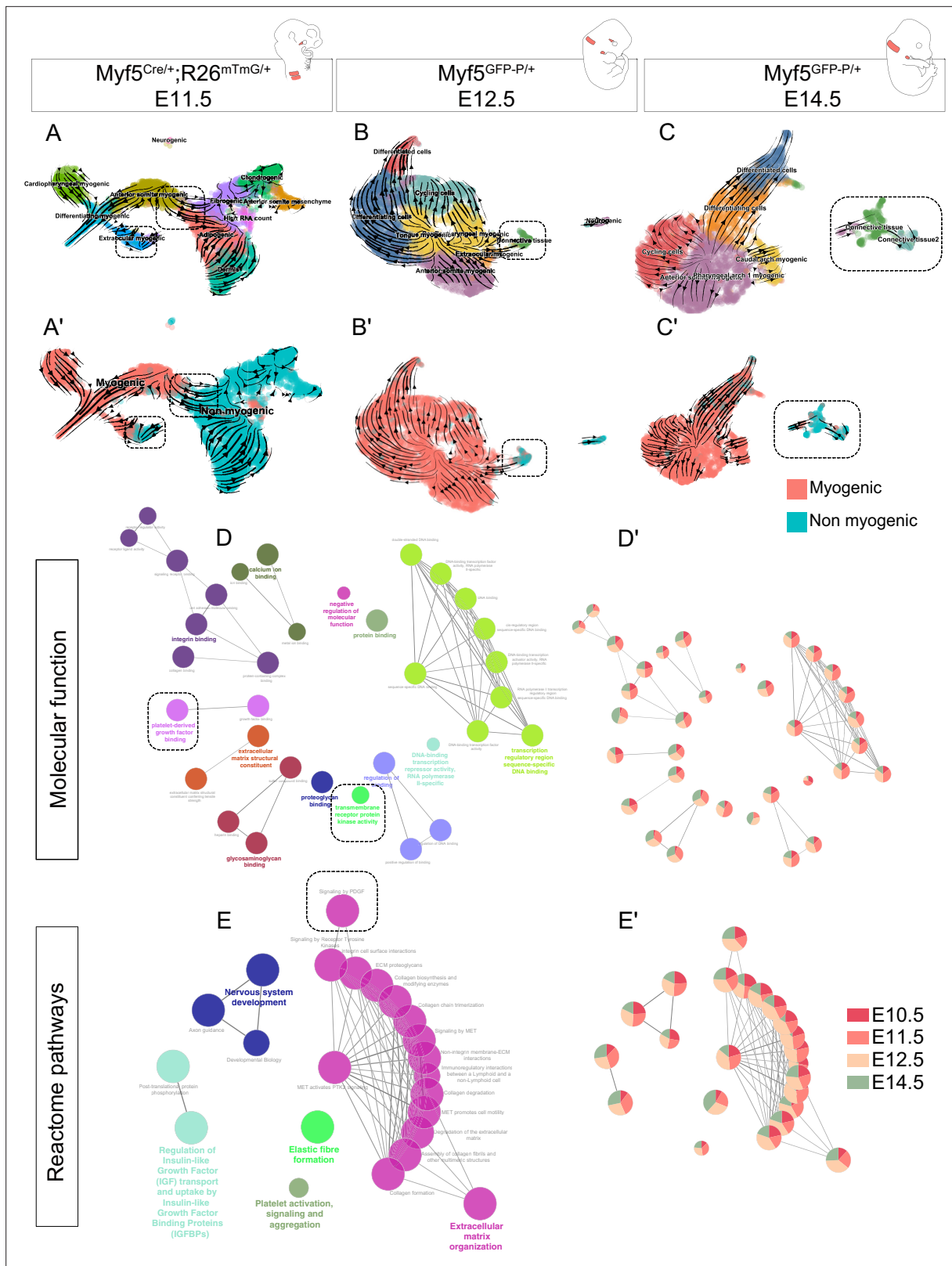


**Figure 6.** *Myf5*-derived non-myogenic cells are generated continuously up to fetal stages. (A-C') RNA velocity plots of *Myf5*<sup>Cre/+</sup>; *Rosa26*<sup>mTmG/+</sup> E11.5, *Myf5*<sup>GFP-P/+</sup> E12.5 and *Myf5*<sup>GFP-P/+</sup> E14.5 datasets (n = 2 pooled datasets, n = 1 embryo and n = 1 embryo, respectively) displaying cell-type annotation (A-C) and myogenic and non-myogenic clustering (A'-C'). The dotted boxes highlight the transitions to non-myogenic clusters in each dataset. (D-E) Gene ontology network of GO Molecular Function and Reactome pathway performed on combined top 100 markers using Cluego. These terms

Figure 6 continued on next page

Figure 6 continued

were generated using the sum of all differentially expressed genes of the non-myogenic clusters across all datasets (see Materials and methods). (D'-E') Relative contribution of each stage to term node represented as piecharts (i.e. the proportion of genes underlying this term coming from that stage). Dotted boxes highlight the shared tyrosine kinase and PDGF signaling pathways.

The online version of this article includes the following figure supplement(s) for figure 6:

**Figure supplement 1.** FACS strategy, preprocessing metrics, expression patterns, and RNA velocity metrics in the *Myf5<sup>GFP-P/+</sup>* E12.5 dataset.

**Figure supplement 2.** FACS strategy, preprocessing metrics, expression patterns and RNA velocity metrics in the *Myf5<sup>GFP-P/+</sup>* E14.5 dataset.

**Figure supplement 3.** Non-myogenic *Myf5*-derived cells display a similar gene ontology.

Here, we also identified a core set of transcription factors specifically active in the non-myogenic cells across all datasets. We propose that these genes guide bipotent cells to a non-myogenic fate and thus confer mesenchymal properties to non-committed progenitors. Recent studies have identified anatomically distinct fibroblastic populations using single-cell transcriptomics, yet unique markers could not be identified (Muhl et al., 2020; Sacchetti et al., 2016), making characterisation of cell subtypes challenging. *Tcf4/Tcf712* was identified as a master regulator of fibroblastic fate during muscle-associated connective tissue development, although it is also expressed in myogenic progenitors at lower levels (Kardon et al., 2003; Mathew et al., 2011; Sefton and Kardon, 2019). We also report that this gene is one of the main regulators of connective tissue fate. Other transcription factors have been linked to skin fibroblast fates including *Tcf4*, *Six2*, *Meox2*, *Egr2*, and *Foxs1*, and their repression favors a myofibroblastic potential (Noizet et al., 2016). *Six2* and *Meox2* were also identified in our analysis, which raises the question of the shared genetic programs between myofibroblastic cells and fibroblastic cells derived from progenitors primed for myogenesis during development.

Interestingly, *Prrx1*, a marker for lateral plate mesoderm (Durland et al., 2008), was differentially expressed in the connective tissue population at various stages. Although lateral plate mesoderm is identifiable in the trunk, its anterior boundaries in the head are unclear (Prummel et al., 2020). More detailed analyses of *Prrx1*, *Isl1*, and *Myf5* lineages need to be carried out to delineate the specific boundaries of each progenitor contribution to cranial connective tissues.

Kinase receptors have been implicated in a number of developmental programs for both muscle and associated connective tissues (Arnold et al., 2020; Knight and Kothary, 2011; Olson and Soriano, 2009; Tallquist et al., 2000; Tzahor et al., 2003; Vinagre et al., 2010). For example, the differentiation of fetal myoblasts is inhibited by growth factors *Tgfb* and *Bmp4* (Cossu et al., 2000). *Epha7* signaling is active in embryonic and adult myocytes and promotes their differentiation (Arnold et al., 2020). Significantly, we noticed a striking and lasting complementary expression of *Pdgfa* and *Pdgfra* throughout embryonic stages, in the myogenic and non-myogenic progenitors respectively. *Pdgf* ligands emanating from hypaxial myogenic cells under the control of *Myf5* were shown to be necessary from rib cartilage development (Tallquist et al., 2000; Vinagre et al., 2010). Additionally, *Pdgfra* promotes expansion of fibroblasts during fibrosis (Olson and Soriano, 2009). Interestingly, we found that *Pdgfa* expression was reduced in cells expressing high levels of *Myog* at the fetal stage (Figure 6—figure supplement 2C). Therefore, *Myf5*-derived myogenic progenitor cells might guide non-myogenic *Myf5*-derived expansion, which in turn provides ligands and extracellular matrix components to favor myogenic development and patterning. Moreover, unlike trunk myogenesis, cranial muscle development relies on the expression of *Wnt* and *Bmp* inhibitors from surrounding tissues (Tzahor et al., 2003). Interestingly, we showed that the *Myf5*-derived non-myogenic cells express *Bmp4*, *Dkk2*, and *Axin2*. Additionally, we showed that the *Wnt* effector complex *Tcf/Lef* is expressed to a lower extent in these cells. It is thus likely that these cells maintain their non-myogenic fate by promoting *Bmp* production and *Wnt* activity cell-autonomously.

Of note, another study suggested shared fate relationships between fibroblast connective tissue cells and skeletal muscle where fibroblastic cells commit to myogenic fate during limb development (Esteves de Lima et al., 2021). Regarding the possibility that some non-myogenic cells may retain bipotent characteristics, our data suggests that the opposite is true during cranial muscle development. First, RNA velocity analysis did not reveal transitioning cells from non-myogenic clusters to myogenic (even at early stages), nor do they express myogenic markers. Further, at least some of these non-myogenic cells gave rise to chondrocytes, which to our knowledge has never been shown to give rise to skeletal muscle. Additionally, bipotency appears to be more associated with myogenic

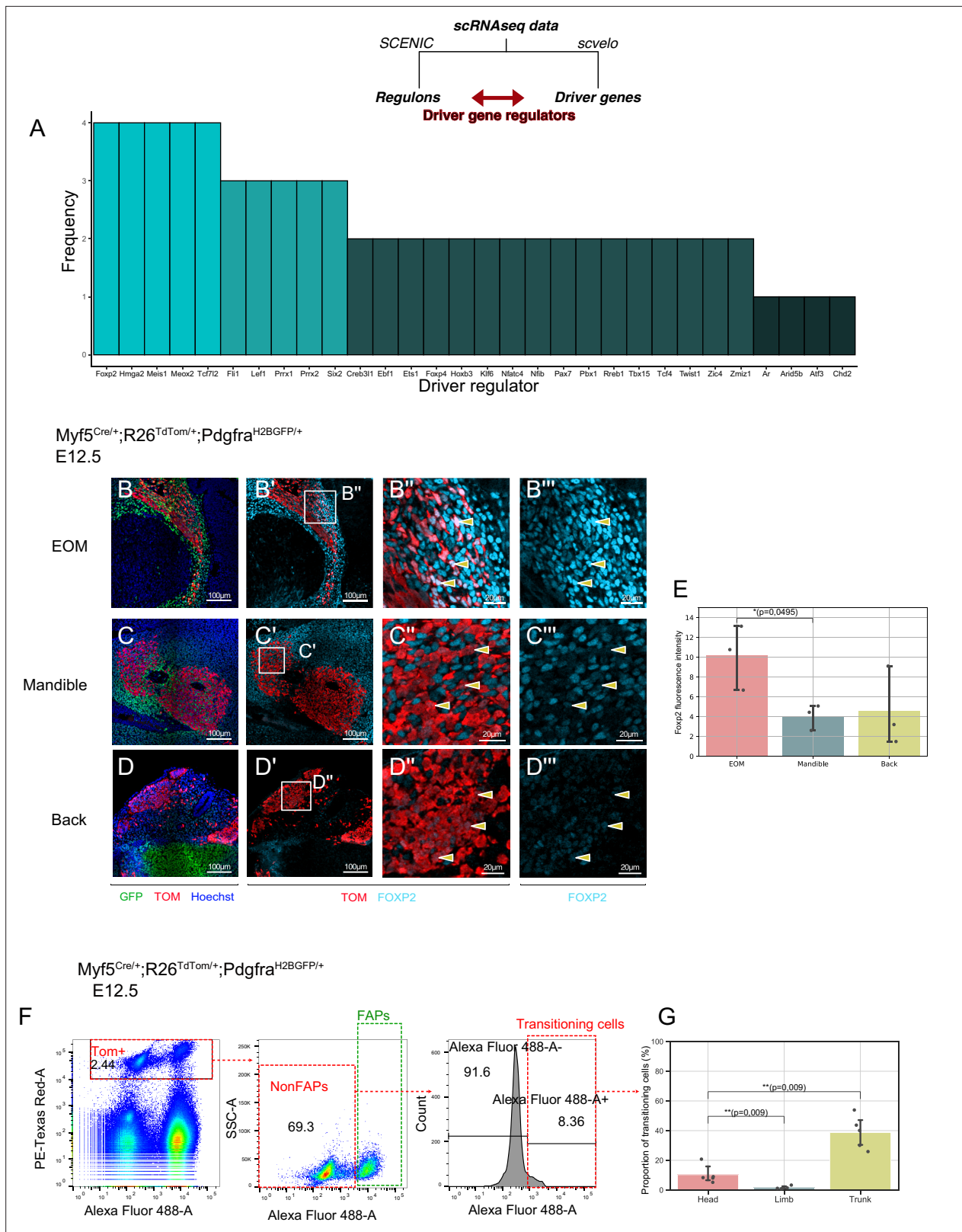


**Figure 7.** A shared program involving Forkhead-box transcription factors supports non-myogenic fate transition at various stages and anatomical locations. **(A)** Barplot displaying frequency of appearance of most predominant transcription factors as driver regulators (4 = present in all four datasets as driver regulon, 1 = present in a single dataset). **(B-D'')** Transverse sections of an E12.5 Myf5<sup>Cre/+</sup>; Rosa26<sup>TdTomato/+</sup>; Pdgfra<sup>H2BGFP/+</sup> embryo immunostained for Foxp2 at the level of the EOM **(B-B'')**, Mandibular muscles **(C-C'')**, and Back muscles **(D-D'')**. Yellow arrowheads indicated the double positive cells

Figure 7 continued on next page

Figure 7 continued

to better appreciate Foxp2 intensity in *Myf5*-derived cells. (E) Quantification of Foxp2 signal intensity in TOM+ (*Myf5*-derived) cells in each muscle (n = 3 embryos). Statistical test performed: Mann-Whitney U test. (F) FACS plots of dissected E12.5 *Myf5<sup>Cre/+</sup>; Rosa26<sup>TdTomato/+</sup>; Pdgfra<sup>H2BGFP/+</sup>* embryos (head region here) highlighting the *Myf5*-derived GFP- TOM+ population transitioning to the GFP+ TOM+ population. Each plot was generated on the population gated in the previous one ('Singlets', 'TOM+' and 'NonFaps'). FAPS: Fibroadipogenic progenitors, a denomination for resident *Pdgfra*+ cells. (G) Quantification of the transitioning population in Head, Limb and Trunk. Proportion of transitioning cells is calculated as the number of Alexa488+/ Total cell number in the 'NonFaps' gate. Note that the Head region is mostly populated by muscles embedded in neural crest (n = 5 embryos). TOM: TdTOMATO.

The online version of this article includes the following source data and figure supplement(s) for figure 7:

**Source data 1.** Excel table summarizing the quantification displayed on **Figure 7E**.

**Source data 2.** Excel table summarizing the quantification displayed on **Figure 7G**.

**Figure supplement 1.** Wnt/ $\beta$ -cat positive feedback loop may promote non-myogenic cell fate.

**Figure supplement 2.** Model of *Myf5*+ bipotent progenitors giving rise to muscle and associated connective tissues.

cells since they express *Myf5*, and to a minor extent *Myod*. Finally, we did not observe NCC-derived *Myf5*+ cells indicating that connective tissue in the head does not give rise to muscle. Nevertheless, to formally exclude the possibility of connective tissue progenitors giving rise to muscle in the embryo, analysis of appropriate markers would need to be done (ex. *Pdgfra*-driven lineage). Further studies should provide insights into the evolutionary ancestry of progenitors that bifurcate to give rise to myogenic and connective tissue cells by studying other model organisms that are devoid of neural crest cells.

## Materials and methods

### Key resources table

Reagent type (species) or resource	Designation	Source or reference	Identifiers	Additional information
Strain, strain background ( <i>Mus musculus</i> )	B6D2F1/JRj	Janvier		
Genetic reagent ( <i>M. musculus</i> )	<i>Myf5<sup>Cre</sup></i>	PMID:17418413	MGI:3710099	Dr. Mario R Capecchi (Institute of Human Genetics, University of Utah, USA)
Genetic reagent ( <i>M. musculus</i> )	<i>Wnt1<sup>Cre</sup></i>	PMID:9843687	MGI:J:69326	Pr. Andrew P. McMahon (Keck School of Medicine of the University of Southern California, USA)
Genetic reagent ( <i>M. musculus</i> )	<i>Mesp1<sup>Cre</sup></i>	PMID:10393122	MGI:2176467	Pr. Yumiko Saga (National Institute of Genetics, Japan)
Genetic reagent ( <i>M. musculus</i> )	<i>Myf5<sup>nlacZ</sup></i>	PMID:8918877	MGI:1857973	Dr. Shahragim Tajbakhsh (Department of Developmental and Stem Cell Biology, Institut Pasteur, France)
Genetic reagent ( <i>M. musculus</i> )	<i>Rosa26<sup>TdTomato</sup></i>	PMID:20023653	MGI:3809524	Dr. Hongkui Zeng (Allen Institute for Brain Science, USA)
Genetic reagent ( <i>M. musculus</i> )	<i>Rosa26<sup>mt/mG</sup></i>	PMID:17868096	MGI:3716464	Pr. Philippe Soriano (Icahn School of Medicine at Mt. Sinai, USA)
Genetic reagent ( <i>M. musculus</i> )	<i>Pdgfra<sup>H2BGFP</sup></i>	PMID:12748302	MGI:2663656	Pr. Philippe Soriano (Icahn School of Medicine at Mt. Sinai, USA)
Genetic reagent ( <i>M. musculus</i> )	<i>Myod<sup>Cre</sup></i>	PMID:19464281	MGI:3840216	Pr. David Goldhamer (University of Connecticut, USA)
Genetic reagent ( <i>M. musculus</i> )	<i>Myf5<sup>GFP-P</sup></i>	PMID:15386014	MGI:3055340	Dr. Shahragim Tajbakhsh (Department of Developmental and Stem Cell Biology, Institut Pasteur, France)
Chemical compound, drug	Sucrose, for molecular biology, $\geq$ 99.5% (GC)	Sigma-Aldrich	S0389-500G	
Chemical compound, drug	Gelatin	Sigma-Aldrich	G-7041	

Continued on next page



Continued

Reagent type (species) or resource	Designation	Source or reference	Identifiers	Additional information
Antibody	Anti-Foxp2 5C11A8 (Mouse monoclonal)	Santa Cruz	SC-517261	IF (1:200)
Antibody	Anti- $\beta$ -gal (Chicken polyclonal)	Abcam	Cat. #: ab9361 RRID:AB_307210	IF (1:1000)
Antibody	Anti- $\beta$ -gal (Rabbit polyclonal)	MP Biomedicals	Cat. #: MP 559761 RRID:AB_2687418	IF (1:1500)
Antibody	Anti-GFP (Chicken polyclonal)	Aves Labs	Cat. #: 1020 RRID:AB_10000240	IF (1:500)
Antibody	Anti-GFP (Chicken polyclonal)	Abcam	Cat. #: 13970 RRID:AB_300798	IF (1:1000)
Antibody	Anti-Myod (Mouse monoclonal)	Dako	Cat. #: M3512 RRID:AB_2148874	IF (1:100)
Antibody	Anti-Myod (Mouse monoclonal)	BD-Biosciences	Cat. #: 554130 RRID:AB_395255	IF (1:500)
Antibody	Anti-Pax7 (Mouse monoclonal)	DSHB	Cat. #: Pax7 RRID:AB_528428	IF (1:20)
Antibody	Anti-Myog (Mouse monoclonal)	DSHB	Cat. #: F5D RRID:AB_2146602	IF (1:20)
Antibody	Alexa Fluor 633 F(ab') <sub>2</sub> Fragment of Goat Anti-Rabbit IgG (H + L) (polyclonal antibody)	Life Technologies	Cat. #: A-21072 RRID:AB_2535733	IF (1:500)
Antibody	Alexa Fluor 555 F(ab') <sub>2</sub> Fragment of Goat Anti-Rabbit IgG (H + L) (polyclonal antibody)	Life Technologies	Cat. #: A-21430 RRID:AB_2535851	IF (1:500)
Antibody	Alexa Fluor 488 F(ab') <sub>2</sub> Fragment of Goat Anti-Rabbit IgG (H + L) (polyclonal antibody)	Life Technologies	Cat. #: A-11070 RRID:AB_2534114	IF (1:500)
Antibody	Alexa Fluor 633 Goat Anti-Chicken IgG (H + L) (polyclonal antibody)	Life Technologies	Cat. #: A-21103 RRID:AB_2535756	IF (1:500)
Antibody	Alexa Fluor 488 Goat Anti-Chicken IgG (H + L) (polyclonal antibody)	Life Technologies	Cat. #: A-11039 RRID:AB_2534096	IF (1:500)
Antibody	Alexa Fluor 633 Goat Anti-Mouse IgG1 ( $\gamma$ 1) (polyclonal antibody)	Life Technologies	Cat. #: A-21126 RRID:AB_2535768	IF (1:500)
Antibody	Alexa Fluor488 AffiniPure Goat Anti-Mouse IgG1 ( $\gamma$ 1) (polyclonal antibody)	Jackson ImmunoResearch	Cat. #: 115-545-205 RRID:AB_2338854	IF (1:500)
Antibody	Cy3-AffiniPure Goat Anti-Mouse IgG1 ( $\gamma$ 1) (polyclonal antibody)	Jackson ImmunoResearch	Cat. #: 115-165-205 RRID:AB_2338694	IF (1:500)
Antibody	Cy3-AffiniPure Goat Anti-Mouse IgG2a ( $\gamma$ 2a) (polyclonal antibody)	Jackson ImmunoResearch	Cat. #: 115-165-206 RRID:AB_2338695	IF (1:500)
Antibody	Dylight 405 Goat Anti-Mouse IgG2a ( $\gamma$ 2a) (polyclonal antibody)	Jackson ImmunoResearch	Cat. #: 115-475-206 RRID:AB_2338800	IF (1:500)
Commercial assay, kit	Hoechst 33,342	Thermo Scientific	Cat. #:H3570	
Commercial assay, kit	RNAscope Multiplex Fluorescent reagent Kit-V2	ACD/Bio-techne	Cat. #: 323100	
Commercial assay, kit	RNAscope H202 & Protease Plus Reagents	ACD/Bio-techne	Cat #: 322330	
Commercial assay, kit	Opal 650 Reagent Pack	PerkinElmer	Cat. #: FP1496001KT	1:1,500 of reconstituted reagent in RNAscope Multiplex TSA Buffer
Commercial assay, kit	Opal 570 Reagent Pack	PerkinElmer	Cat. #: FP1488001KT	1:1,500 of reconstituted reagent in RNAscope Multiplex TSA Buffer
Commercial assay, kit	RNAscope Mm-Pdgfa	Advanced Cell Diagnostics, Inc	Cat #:411361	
Commercial assay, kit	RNAscope Mm-Pdgfra	Advanced Cell Diagnostics, Inc	Cat #:480661-C2	
Commercial assay, kit	RNAscope Mm-Bmpr1b	Advanced Cell Diagnostics, Inc	Cat #:533941	

Continued on next page

Continued

Reagent type (species) or resource	Designation	Source or reference	Identifiers	Additional information
Commercial assay, kit	RNAscope Mm-Efnb1	Advanced Cell Diagnostics, Inc	Cat #:526761	
Commercial assay, kit	RNAscope Mm-Bmp4-O1-C3	Advanced Cell Diagnostics, Inc	Cat #:527501-C3	
Commercial assay, kit	RNAscope Mm-Ephb1-C3	Advanced Cell Diagnostics, Inc	Cat #:567571-C3	
Commercial assay, kit	RNAscope Mm-Scube1	Advanced Cell Diagnostics, Inc	Cat #:488131	
Chemical compound, drug	Paraformaldehyde	Electron Microscopy Sciences	Cat. #: 15710	
Chemical compound, drug	Isopentane	VWR	Cat. #: 24872.298	
Chemical compound, drug	Triton X-100	Sigma	Cat. #: T8787	
Chemical compound, drug	Tween 20	Sigma	Cat. #: P1379	
Chemical compound, drug	TrypLE	ThermoFisher	Cat #: 12604013	
Chemical compound, drug	Calcein Blue	eBioscience	Cat #: 65-0855-39	
Chemical compound, drug	Propidium Iodide	ThermoFisher	Cat #: P1304MP	
Commercial assay, kit	Chromium Next GEM Chip G Single Cell Kit, 16 rxns	10 X Genomics	Cat #: 1000127	
Commercial assay, kit	Chromium Next GEM Single Cell 3' GEM, Library & Gel Bead Kit v3.1, 4 rxns	10 X Genomics	Cat #:1000128	
Commercial assay, kit	NextSeq 500/550 High Output Kit v2.5	Illumina	Cat #: 20024906	
Commercial assay, kit	Agilent High Sensitivity DNA Kit	Agilent	Cat #:5067-4626	
Commercial assay, kit	Agilent High Sensitivity DNA Reagents	Agilent	Cat #:5067-4627	
Commercial assay, kit	Qubit dsDNA HS Assay Kit	Life Technologies	Cat #:Q32854	
Software, algorithm	RStudio	Rstudio		
Software, algorithm	Anaconda	Anaconda Inc		
Software, algorithm	Zen	Zeiss		
Software, algorithm	Cytoscape	Cytoscape Team		
Software, algorithm	Fiji	Johannes Schindelin, Ignacio Arganda-Carreras, Albert Cardona, Mark Longair, Benjamin Schmid, and others		
Software, algorithm	Prism	GraphPad Software		
Software, algorithm	FlowJo	FlowJo		

## scRNAseq data generation

For E10.5 to E12.5 embryos, the cranial region above the forelimb was dissected in ice-cold 3% FBS in PBS and mechanically dissociated with forceps and pipetting. The same procedure was applied at E14.5 but the dissection was refined to the pharyngeal and laryngeal regions. Tissues were then digested in TrypLE (ThermoFisher Cat #: 12604013) during 3 rounds of 5 min incubation (37 °C, 1400 RPM), interspersed with gentle pipetting to further dissociate the tissue. Cells were resuspended in FBS 3%, filtered, and incubated with Calcein Blue (eBioscience, Cat #: 65-0855-39) and Propidium Iodide (ThermoFisher Cat #: P1304MP) to check for viability. Viable cells were sorted on BD FACS Aria III and manually counted using a hemocytometer. RNA integrity was assessed with Agilent Bioanalyzer 2,100 to validate the isolation protocol prior to scRNAseq (RIN >8 was considered acceptable). A total of 4000–13,000 cells were loaded onto 10 X Genomics Chromium microfluidic chip and cDNA libraries were generated following manufacturer's protocol. Concentrations and fragment sizes were measured using Agilent Bioanalyzer and Invitrogen Qubit. cDNA libraries were sequenced using NextSeq 500 and High Output v2.5 (75 cycles) kits. Genome mapping and count matrix generation were done following 10X Genomics Cell Ranger pipeline.

**Table 2.** Driver regulators of non-myogenic fate in each dataset.

	E10.5	E11.5	E12.5	E14.5
Foxp2	(+)	(+)	(+)	(+)
Hmga2	(+)	(+)	(+)	(+)
Meis1	(+)	(+)	(+)	(+)
Meox2	(+)	(+)	(+)	(+)
Tcf7l2	(+)	(+)	(+)	(+)
Fli1	(+)	(+)	(+)	(-)
Lef1	(-)	(+)	(+)	(+)
Prrx1	(+)	(+)	(-)	(+)
Prrx2	(-)	(+)	(+)	(+)
Six2	(+)	(+)	(+)	(-)
Creb3l1	(-)	(+)	(-)	(+)
Ebf1	(+)	(-)	(+)	(-)
Ets1	(-)	(+)	(-)	(+)
Foxp4	(+)	(+)	(-)	(-)
Hoxb3	(-)	(+)	(+)	(-)
Klf6	(-)	(+)	(-)	(+)
Nfatc4	(-)	(+)	(-)	(+)
Nfib	(-)	(+)	(+)	(-)
Pax7	(-)	(-)	(+)	(+)
Pbx1	(-)	(+)	(-)	(+)
Rreb1	(-)	(-)	(+)	(+)
Tbx15	(+)	(+)	(-)	(-)
Tcf4	(+)	(-)	(+)	(-)
Twist1	(+)	(+)	(-)	(-)
Zic4	(+)	(-)	(+)	(-)
Zmiz1	(-)	(+)	(+)	(-)
Ar	(-)	(-)	(-)	(+)
Arid5b	(-)	(-)	(+)	(-)
Atf3	(-)	(-)	(-)	(+)
Chd2	(+)	(-)	(-)	(-)

(+): Present, (-): Absent.

E14.5), no replicates were used. Annotation and subsetting were also performed in Seurat. ‘Myogenic’ and ‘Non-myogenic’ annotations were based on *Pdgfa* and *Pdgfra* expression and myogenic genes *Myf5*, *Myod*, and *Myog*. Cells not expressing *Pdgfa* were annotated as ‘non-myogenic’ unless they express myogenic genes. Cells expressing *Pdgfa* were annotated as ‘myogenic’. We noticed that at later stages, *Pdgfa* expression decreases in Myog+ cells. Driver genes of connective tissue at E12.5 and E14.5 were determined using cluster annotations obtained from Leiden-based clustering. Myogenic and non-myogenic scores were generated by aggregating the total expression of all genes

## RNA velocity and driver genes

RNA velocity analyses were performed using scvelo (Bergen et al., 2020) in Python. This tool allows inferring velocity flow and driver genes using scRNAseq data, with major improvements from previous methods (La Manno et al., 2018). First, unspliced and spliced transcript matrices were generated using velocity (La Manno et al., 2018) command line function, which outputs unspliced, spliced, and ambiguous matrices as a single loom file. These files were combined with filtered Seurat objects to yield objects with unspliced and spliced matrices, as well as Seurat-generated annotations and cell-embeddings (UMAP, tSNE, PCA). These datasets were then processed following scvelo online guide and documentation. Velocity was calculated based on the dynamical model (using `scv.tl.recover_dynamics(adata)`, and `scv.tl.velocity(adata, mode='dynamical')`) and when outliers were detected, differential kinetics based on top driver genes were calculated and added to the model (using `scv.tl.velocity(adata, diff_kinetics = True)`). Specific driver genes were identified by determining the top likelihood genes in the selected cluster. The lists of top 100 drivers for each stage are given in Table 1.

## Data processing

scRNAseq datasets were preprocessed using Seurat in R (<https://satijalab.org/seurat/>) (Butler et al., 2018). Cells with more than 20% of mitochondrial gene fraction were discarded. The number of genes expressed averaged to 4000 in all four datasets. Dimension reduction and UMAP generation were performed following Seurat workflow. Doublets were inferred using DoubletFinder v3 (McGinnis et al., 2019). Cell cycle genes, mitochondrial fraction, number of genes, number of UMI were regressed in all datasets following Seurat dedicated vignette. We noticed that cell cycle regression, although clarifying anatomical diversity, seemed to induce low and high UMI clustering (Figure 4A, Figure 4—figure supplement 1C). For the E10.5 and E11.5 datasets, two replicates were generated from littermates and merged after confirming their similitude. For subsequent datasets (E12.5 and

in a signature based on the top 10 markers of these compartments (visible on **Figure 4C**). Each score was then divided by the sum of the two to generate myogenic and non-myogenic signatures. The coexpression score was defined by the product of these signatures. To generate the plots, cells were ordered based on their non-myogenic signature. The 'transition' was defined as cells with a coexpression score higher than 0.20.

## Gene regulatory network inference

Gene regulatory networks were inferred using SCENIC (R implementation) (Aibar et al., 2017) and pySCENIC (Python implementation) (Van de Sande et al., 2020). This algorithm allows regrouping of sets of correlated genes into regulons (i.e. a transcription factor and its targets) based on motif binding and co-expression. UMAP and heatmap were generated using regulon AUC matrix (Area Under Curve) which refers to the activity level of each regulon in each cell. We used two cisTarget databases: 'mm9-500bp-upstream-7species.mc9nr' (500 bp upstream of TSS) and 'mm9-tss-centered-10kb-7species.mc9nr' (10kb  $\pm$ TSS).

## Driver regulons

Results from SCENIC and scvelo were combined to identify regulons that could be responsible for the transcriptomic induction of driver genes. Similarly to the steps mentioned above, SCENIC lists of regulons were used to infer connections between transcription factors and driver gene. Networks were generated as explained above and annotated with 'Active regulon' or 'driver gene'. The lists of individual driver regulons of each dataset were then combined and the most recurring driver regulons were identified. The code is available at this address: <https://github.com/TajbakhshLab/DriverRegulators>, (copy archived at [swh:1:rev:49db57e7ede9f248de937b7a47eb96b02aa2ce67](https://www.swh.io/rev/49db57e7ede9f248de937b7a47eb96b02aa2ce67); Grimaldi, 2021).

## Gene set enrichment analysis

Gene set enrichment analyses were performed on either the top markers (obtained from Seurat function FindAllMarkers) or from driver genes (obtained from scvelo), using Cluego (Bindea et al., 2009). 'GO Molecular Pathway', 'GO Biological Process' and 'Reactome pathways' were used independently to identify common and unique pathways involved in each dataset. In all analyses, an enrichment/depletion two-sided hypergeometric test was performed and p-values were corrected using the Bonferroni step down method.

## Mouse strains

Animals were handled as per European Community guidelines and the ethics committee of the Institut Pasteur (CETEA) approved protocols (APAFIS#6354–20160809 I2028839). The following strains were previously described: *Myf5<sup>Cre</sup>* (Haldar et al., 2008), *Myod<sup>Cre</sup>* (Kanisicak et al., 2009), *Mesp1<sup>Cre</sup>* (Saga et al., 1999), *Tg:Wnt1Cre* (Danielian et al., 1998), *Rosa26<sup>TdTom</sup>* (Ai9; Madisen et al., 2010), *Rosa26<sup>mTmG</sup>* (Muzumdar et al., 2007), *Myf5<sup>nlacZ</sup>* (Tajbakhsh et al., 1996), *Pdgfra<sup>H2BGFP</sup>* (Hamilton et al., 2003) and *Myf5<sup>GFP-P</sup>* (Kassar-Duchossoy et al., 2004). To generate *Myf5<sup>Cre/+</sup>;Rosa26<sup>TdTomato/+</sup>;Pdgfra<sup>H2BGFP/+</sup>* embryos, *Myf5<sup>Cre/+</sup>* females were crossed with *Pdgfra<sup>H2BGFP/+</sup>;Rosa26<sup>TdTomato/TdTomato</sup>* males. Mice were kept on a mixed genetic background C57BL/6JRj and DBA/2JRj (B6D2F1, Janvier Labs). Mouse embryos and fetuses were collected between embryonic day (E) E10.5 and E14.5, with noon on the day of the vaginal plug considered as E0.5.

## Immunofluorescence

Collected embryonic and adult tissues were fixed 2.5 h in 4% paraformaldehyde (Electron Microscopy Sciences, Cat #:15710) in PBS with 0.2–0.5% Triton X-100 (according to their stage) at 4 °C and washed overnight at 4 °C in PBS. In preparation for cryosectioning, embryos were equilibrated in 30% sucrose in PBS overnight at 4 °C and embedded in OCT. Cryosections (16–20  $\mu$ m) were left to dry at RT for 30 min and washed in PBS. For Foxp2 immunostaining (Santa Cruz Cat. #: SC-517261), embryos were first equilibrated in 15% sucrose overnight, then in a 15% sucrose/7.5% gelatin solution at 37 °C the next day and embedded in the same solution the following day. Blocks were then kept at 4 °C in a humid environment and trimmed, before being submerged in liquid nitrogen-cooled isopentane at –60 °C to freeze. After cryosectioning, slides were washed twice for 15 min each at 37 °C in PBS to remove the gelatin. The primary antibodies used in this study are chicken polyclonal

anti- $\beta$ -gal (Abcam, Cat #: ab9361, dilution 1:1000), mouse monoclonal IgG1 anti-Myod (BD Biosciences, Cat# 554130, dilution 1:100), mouse monoclonal IgG1 anti-Pax7 (DSHB, Cat. #: AB\_528428, dilution 1:20), rabbit anti-mouse Sox9 (Millipore, Cat. #: AB5535, dilution 1/2000), rabbit polyclonal anti-Tomato (Clontech Cat. #: 632496, dilution 1:400) and chicken polyclonal anti-GFP (Abcam Cat. #: 13970, dilution 1:1000). Images were acquired using Zeiss LSM780 or LSM700 confocal microscopes and processed using ZEN software (Carl Zeiss). Control and mutant embryos were selected randomly, quantifications were performed blindly by hiding the discriminating channels. Quantifications were performed using Fiji (<https://imagej.net/software/fiji/>). Barplots, dotplots and boxplots were generated using Seaborn (<https://seaborn.pydata.org/>; <https://seaborn.pydata.org/>) or Prism (<https://www.graphpad.com/scientific-software/prism/>). For the *Myf5<sup>Cre/+</sup>;Rosa26<sup>TdTomato/+</sup>;Pdgfra<sup>H2BGFP/+</sup>* embryos, 4 regions were manually defined across the medio-lateral axis. For each region, the absolute number of double-positive cells within the defined area was divided by the total number of GFP+ cells which was determined first, and blindly (with the TOMchannel disabled). For the *Myod<sup>flCre</sup>* lineage-tracing experiment, the absolute number of double positive cells were counted and divided by the area of the muscle given by the TOM channel. These 'number of cells/area' scores were then corrected based on the size of the image in microns, and adjusted to match an area of 100  $\mu\text{m}^2$  of muscle. To quantify the intensity of Foxp2 immunostaining, we first generated ROIs of the *Myf5*-derived cells based on the TOM channels as previously mentioned and extracted the mean pixel value. All images were acquired using the exact same settings for a given embryo.

## RNAscope in situ hybridization

Embryos for in situ hybridization were fixed overnight in 4% PFA. Embryos were equilibrated in 30% sucrose in PBS and sectioned as described for immunofluorescence. RNAscope probes Mm-Pdgfra (411361), Mm-Pdgfra (480661-C2), Mm-Bmpr1b (533941), Mm-Efnb1 (526761), Mm-Bmp4-O1-C3 (527501-C3), Mm-Ephb1-C3 (567571-C3) and Mm-Scube1 (488131) were purchased from Advanced Cell Diagnostics, Inc. In situ hybridization was performed using the RNAscope Multiplex Fluorescent Reagent Kit V2 as described previously (Comai et al., 2019). Quantifications were performed using Fiji (<https://imagej.net/software/fiji/>). 2 ROIs were first defined visually using the GFP channel: 'myogenic' and 'non-myogenic'. The channels containing the RNAscope signals were then thresholded to obtain binary images, and measurement of the 'Area%' was performed for each ROI. For each probe, we generated a ratio of myogenic to non-myogenic signal. The ratio of each receptor was then subtracted from the ratio of each corresponding ligand.

## Acknowledgements

We acknowledge funding support from the Institut Pasteur, Association Française contre le Myopathies, Agence Nationale de la Recherche (Laboratoire d'Excellence Revive, Investissement d'Avenir; ANR-10-LABX-73) and MyoHead (ANR-19-CE13-0008-01), Association Française contre les Myopathies (Grant #20510), Fondation pour la Recherche Médicale (Grant # FDT201904008277), and the Centre National de la Recherche Scientifique. We gratefully acknowledge the UtechS Photonic BioImaging, C2RT, Institut Pasteur, supported by the French National Research Agency (France BioImaging; ANR-10-INSB-04; Investments for the Future).

## Additional information

### Competing interests

Shahragim Tajbakhsh: Reviewing editor, eLife. The other authors declare that no competing interests exist.

### Funding

Funder	Grant reference number	Author
Association Française contre les Myopathies	20510	Alexandre Grimaldi



Funder	Grant reference number	Author
Fondation pour la Recherche Médicale	FDT201904008277	Alexandre Grimaldi
Agence Nationale de la Recherche	ANR-10-LABX-73	Shahragim Tajbakhsh
Centre National de la Recherche Scientifique		Glenda Comai
Agence Nationale de la Recherche	ANR-19-CE13-0008-01	Shahragim Tajbakhsh

The funders had no role in study design, data collection and interpretation, or the decision to submit the work for publication.

### Author contributions

Alexandre Grimaldi, Conceptualization, Data curation, Formal analysis, Funding acquisition, Investigation, Methodology, Project administration, Software, Supervision, Validation, Visualization, Writing – original draft, Writing – review and editing; Glenda Comai, Conceptualization, Formal analysis, Investigation, Validation, Visualization, Writing – review and editing; Sebastien Mella, Data curation, Formal analysis, Software, Writing – review and editing; Shahragim Tajbakhsh, Conceptualization, Funding acquisition, Project administration, Resources, Supervision, Writing – review and editing

### Author ORCIDs

Alexandre Grimaldi  <http://orcid.org/0000-0002-5978-2057>  
 Glenda Comai  <http://orcid.org/0000-0003-3244-3378>  
 Sebastien Mella  <http://orcid.org/0000-0002-8679-5718>  
 Shahragim Tajbakhsh  <http://orcid.org/0000-0003-1809-7202>

### Ethics

Animals were handled as per European Community guidelines and the ethics committee of the Institut Pasteur (CETEA) approved protocols (APAFIS#6354-20160809 I2028839).

### Decision letter and Author response

Decision letter <https://doi.org/10.7554/eLife.70235.sa1>  
 Author response <https://doi.org/10.7554/eLife.70235.sa2>

## Additional files

### Supplementary files

- Transparent reporting form

### Data availability

scRNAseq datasets are available in open access on DRYAD at the following address: <https://data-dryad.org/stash/dataset/doi:10.5061/dryad.gf1vhhmrs?>. The code that was used to generate the driver regulators is available at this address: <https://github.com/TajbakhshLab/DriverRegulators>, (copy archived at [swh:1:rev:49db57e7ede9f248de937b7a47eb96b02aa2ce67](https://www.swh.io/rev/49db57e7ede9f248de937b7a47eb96b02aa2ce67)). Source data files have been provided for Figure 3J, Figure 4H, Figure 5F, Figure 5J, Figure 5-figure supplement 1E, Figure 7E and Figure 7G.

The following dataset was generated:

Author(s)	Year	Dataset title	Dataset URL	Database and Identifier
Grimaldi A, Mella S	2022	scRNAseq_raw_filtered_preprocessed	<a href="https://dx.doi.org/10.5061/dryad.gf1vhhmrs">https://dx.doi.org/10.5061/dryad.gf1vhhmrs</a>	Dryad Digital Repository, 10.5061/dryad.gf1vhhmrs

## References

- Adachi N**, Bilio M, Baldini A, Kelly RG. 2020. Cardiopharyngeal mesoderm origins of musculoskeletal and connective tissues in the mammalian pharynx. *Development (Cambridge, England)* **147**:dev185256. DOI: <https://doi.org/10.1242/dev.185256>, PMID: 32014863
- Aibar S**, González-Blas CB, Moerman T, Huynh-Thu VA, Imrichova H, Hulselmans G, Rambow F, Marine J-C, Geurts P, Aerts J, van den Oord J, Atak ZK, Wouters J, Aerts S. 2017. SCENIC: single-cell regulatory network inference and clustering. *Nature Methods* **14**:1083–1086. DOI: <https://doi.org/10.1038/nmeth.4463>, PMID: 28991892
- Arnold LL**, Cecchini A, Stark DA, Ihnat J, Craigg RN, Carter A, Zino S, Cornelison D. 2020. EphA7 promotes myogenic differentiation via cell-cell contact. *eLife* **9**:e53689. DOI: <https://doi.org/10.7554/eLife.53689>, PMID: 32314958
- Babb R**, Chandrasekaran D, Carvalho Moreno Neves V, Sharpe PT. 2017. Axin2-expressing cells differentiate into reparative odontoblasts via autocrine Wnt/ $\beta$ -catenin signaling in response to tooth damage. *Scientific Reports* **7**:3102. DOI: <https://doi.org/10.1038/s41598-017-03145-6>, PMID: 28596530
- Ben-Yair R**, Kalcheim C. 2008. Notch and bone morphogenetic protein differentially act on dermomyotome cells to generate endothelium, smooth, and striated muscle. *The Journal of Cell Biology* **180**:607–618. DOI: <https://doi.org/10.1083/jcb.200707206>, PMID: 18268106
- Bergen V**, Lange M, Peidli S, Wolf FA, Theis FJ. 2020. Generalizing RNA velocity to transient cell states through dynamical modeling. *Nature Biotechnology* **38**:1408–1414. DOI: <https://doi.org/10.1038/s41587-020-0591-3>, PMID: 32747759
- Biferali B**, Proietti D, Mozzetta C, Madaro L. 2019. Fibro-Adipogenic Progenitors Cross-Talk in Skeletal Muscle: The Social Network. *Frontiers in Physiology* **10**:1074. DOI: <https://doi.org/10.3389/fphys.2019.01074>, PMID: 31496956
- Bildsoe H**, Fan X, Wilkie EE, Ashoti A, Jones VJ, Power M, Qin J, Wang J, Tam PPL, Loebel DAF. 2016. Transcriptional targets of TWIST1 in the cranial mesoderm regulate cell-matrix interactions and mesenchyme maintenance. *Developmental Biology* **418**:189–203. DOI: <https://doi.org/10.1016/j.ydbio.2016.08.016>, PMID: 27546376
- Bindea G**, Mlecnik B, Hackl H, Charoentong P, Tosolini M, Kirilovsky A, Fridman WH, Pagès F, Trajanoski Z, Galon J. 2009. ClueGO: a Cytoscape plug-in to decipher functionally grouped gene ontology and pathway annotation networks. *Bioinformatics (Oxford, England)* **25**:1091–1093. DOI: <https://doi.org/10.1093/bioinformatics/btp101>, PMID: 19237447
- Bothe I**, Dietrich S. 2006. The molecular setup of the avian head mesoderm and its implication for craniofacial myogenesis. *Developmental Dynamics* **235**:2845–2860. DOI: <https://doi.org/10.1002/dvdy.20903>, PMID: 16894604
- Buckingham M**, Rigby PWJ. 2014. Gene regulatory networks and transcriptional mechanisms that control myogenesis. *Developmental Cell* **28**:225–238. DOI: <https://doi.org/10.1016/j.devcel.2013.12.020>, PMID: 24525185
- Burke AC**, Nowicki JL. 2003. A new view of patterning domains in the vertebrate mesoderm. *Developmental Cell* **4**:159–165. DOI: [https://doi.org/10.1016/s1534-5807\(03\)00033-9](https://doi.org/10.1016/s1534-5807(03)00033-9), PMID: 12586060
- Butler A**, Hoffman P, Smibert P, Papalexis E, Satija R. 2018. Integrating single-cell transcriptomic data across different conditions, technologies, and species. *Nature Biotechnology* **36**:411–420. DOI: <https://doi.org/10.1038/nbt.4096>, PMID: 29608179
- Cao J**, Spielmann M, Qiu X, Huang X, Ibrahim DM, Hill AJ, Zhang F, Mundlos S, Christiansen L, Steemers FJ, Trapnell C, Shendure J. 2019. The single-cell transcriptional landscape of mammalian organogenesis. *Nature* **566**:496–502. DOI: <https://doi.org/10.1038/s41586-019-0969-x>, PMID: 30787437
- Christ B**, Huang R, Scaal M. 2007. Amniote somite derivatives. *Developmental Dynamics* **236**:2382–2396. DOI: <https://doi.org/10.1002/dvdy.21189>, PMID: 17557304
- Comai G**, Heude E, Mella S, Paisant S, Pala F, Gallardo M, Langa F, Kardon G, Gopalakrishnan S, Tajbakhsh S. 2019. A distinct cardiopharyngeal mesoderm genetic hierarchy establishes antero-posterior patterning of esophagus striated muscle. *eLife* **8**:e47460. DOI: <https://doi.org/10.7554/eLife.47460>, PMID: 31535973
- Comai GE**, Tesařová M, Dupé V, Rhinn M, Vallecillo-García P, da Silva F, Feret B, Exelby K, Dollé P, Carlsson L, Pryce B, Spitz F, Stricker S, Zikmund T, Kaiser J, Briscoe J, Schedl A, Ghyselinck NB, Schweitzer R, Tajbakhsh S. 2020. Local retinoic acid signaling directs emergence of the extraocular muscle functional unit. *PLOS Biology* **18**:e3000902. DOI: <https://doi.org/10.1371/journal.pbio.3000902>, PMID: 33201874
- Conerly ML**, Yao Z, Zhong JW, Groudine M, Tapscott SJ. 2016. Distinct Activities of Myf5 and MyoD Indicate Separate Roles in Skeletal Muscle Lineage Specification and Differentiation. *Developmental Cell* **36**:375–385. DOI: <https://doi.org/10.1016/j.devcel.2016.01.021>, PMID: 26906734
- Cossu G**, Angelis LD, Borello U, Berarducci B, Buffa V, Sonnino C, Coletta M, Vivarelli E, Bouche M, Lattanzi L, Tosoni D, Donna SD, Berghella L, Salvatori G, Murphy P, Angelis M, Molinaro M. 2000. Determination, diversification and multipotency of mammalian myogenic cells. *Int J Dev Biol* **44**:699–706.
- Danielian PS**, Muccino D, Rowitch DH, Michael SK, McMahon AP. 1998. Modification of gene activity in mouse embryos in utero by a tamoxifen-inducible form of Cre recombinase. *Current Biology* **8**:1323–1326. DOI: [https://doi.org/10.1016/s0960-9822\(07\)00562-3](https://doi.org/10.1016/s0960-9822(07)00562-3), PMID: 9843687
- Daubas P**, Tajbakhsh S, Hadchouel J, Primig M, Buckingham M. 2000. Myf5 is a novel early axonal marker in the mouse brain and is subjected to post-transcriptional regulation in neurons. *Development* **127**:319–331. DOI: <https://doi.org/10.1242/dev.127.2.319>

- De Micheli AJ**, Swanson JB, Dissler NP, Martinez LM, Walker NR, Oliver DJ, Cosgrove BD, Mendias CL. 2020. Single-cell transcriptomic analysis identifies extensive heterogeneity in the cellular composition of mouse Achilles tendons. *American Journal of Physiology. Cell Physiology* **319**:C885–C894. DOI: <https://doi.org/10.1152/ajpcell.00372.2020>, PMID: 32877217
- Devotta A**, Hong CS, Saint-Jeannet JP. 2018. Dkk2 promotes neural crest specification by activating Wnt/ $\beta$ -catenin signaling in a GSK3 $\beta$  independent manner. *eLife* **7**:e34404. DOI: <https://doi.org/10.7554/eLife.34404>, PMID: 30035713
- Diogo R**, Kelly RG, Christiaen L, Levine M, Ziermann JM, Molnar JL, Noden DM, Tzahor E. 2015. A new heart for A new head in vertebrate cardiopharyngeal evolution. *Nature* **520**:466–473. DOI: <https://doi.org/10.1038/nature14435>, PMID: 25903628
- Durland JL**, Sferlazzo M, Logan M, Burke AC. 2008. Visualizing the lateral somitic frontier in the Prx1Cre transgenic mouse. *Journal of Anatomy* **212**:590–602. DOI: <https://doi.org/10.1111/j.1469-7580.2008.00879.x>, PMID: 18430087
- Esteves de Lima J**, Blavet C, Bonnin MA, Hirsinger E, Comai G, Yvernogeu L, Delfini MC, Bellenger L, Mella S, Nassari S, Robin C, Schweitzer R, Fournier-Thibault C, Jaffredo T, Tajbakhsh S, Relaix F, Duprez D. 2021. Unexpected contribution of fibroblasts to muscle lineage as a mechanism for limb muscle patterning. *Nature Communications* **12**:3851. DOI: <https://doi.org/10.1038/s41467-021-24157-x>, PMID: 34158501
- Farahani RM**, Xaymardan M. 2015. Platelet-Derived Growth Factor Receptor Alpha as a Marker of Mesenchymal Stem Cells in Development and Stem Cell Biology. *Stem Cells International* **2015**:362753. DOI: <https://doi.org/10.1155/2015/362753>, PMID: 26257789
- Ferdous A**, Singh S, Luo Y, Abedin MJ, Jiang N, Perry CE, Evers BM, Gillette TG, Kyba M, Trojanowska M, Hill JA. 2021. Fli1 Promotes Vascular Morphogenesis by Regulating Endothelial Potential of Multipotent Myogenic Progenitors. *Circulation Research* **129**:949–964. DOI: <https://doi.org/10.1161/CIRCRESAHA.121.318986>, PMID: 34544261
- Franco H**, Casasnovas JJ, Cadilla CL. 2009. Periostin gene expression is regulated by the bHLH transcription factor TWIST2 in human skin fibroblasts. *The FASEB Journal* **23**:660. DOI: [https://doi.org/10.1096/fasebj.23.1\\_supplement.660.11](https://doi.org/10.1096/fasebj.23.1_supplement.660.11)
- Gans C**, Northcutt RG. 1983. Neural crest and the origin of vertebrates: A new head. *Science (New York, N.Y.)* **220**:268–273. DOI: <https://doi.org/10.1126/science.220.4594.268>, PMID: 17732898
- Grenier J**, Teillet MA, Grifone R, Kelly RG, Duprez D. 2009. Relationship between neural crest cells and cranial mesoderm during head muscle development. *PLOS ONE* **4**:e4381. DOI: <https://doi.org/10.1371/journal.pone.0004381>, PMID: 19198652
- Grimaldi A**, Parada C, Chai Y. 2015. A Comprehensive Study of Soft Palate Development in Mice. *PLOS ONE* **10**:e0145018. DOI: <https://doi.org/10.1371/journal.pone.0145018>, PMID: 26671681
- Grimaldi A**. 2021. TajbakhshLab/DriverRegulators. swb:1:rev:49db57e7ede9f248de937b7a47eb96b02aa2ce67. GitHub. <https://archive.softwareheritage.org/swb:1:dir:8de8228c445b380ce67fd8fb5866a0bcbcd93f3b;origin=https://github.com/TajbakhshLab/DriverRegulators;visit=swb:1:snp:eec9f98b7df6daa821eb336d769afaa6f680803f;anchor=swb:1:rev:49db57e7ede9f248de937b7a47eb96b02aa2ce67>
- Gross MK**, Moran-Rivard L, Velasquez T, Nakatsu MN, Jagla K, Goulding M. 2000. Lbx1 is required for muscle precursor migration along a lateral pathway into the limb. *Development (Cambridge, England)* **127**:413–424. DOI: <https://doi.org/10.1242/dev.127.2.413>
- Haldar M**, Karan G, Tvrdik P, Capecchi MR. 2008. Two cell lineages, myf5 and myf5-independent, participate in mouse skeletal myogenesis. *Developmental Cell* **14**:437–445. DOI: <https://doi.org/10.1016/j.devcel.2008.01.002>, PMID: 18331721
- Hamilton TG**, Klinghoffer RA, Corrin PD, Soriano P. 2003. Evolutionary divergence of platelet-derived growth factor alpha receptor signaling mechanisms. *Molecular and Cellular Biology* **23**:4013–4025. DOI: <https://doi.org/10.1128/MCB.23.11.4013-4025.2003>, PMID: 12748302
- He P**, Williams BA, Trout D, Marinov GK, Amrhein H, Berghella L, Goh ST, Plajzer-Frick I, Afzal V, Pennacchio LA, Dickel DE, Visel A, Ren B, Hardison RC, Zhang Y, Wold BJ. 2020. The changing mouse embryo transcriptome at whole tissue and single-cell resolution. *Nature* **583**:760–767. DOI: <https://doi.org/10.1038/s41586-020-2536-x>, PMID: 32728245
- Heude E**, Tesarova M, Sefton EM, Jullian E, Adachi N, Grimaldi A, Zikmund T, Kaiser J, Kardon G, Kelly RG, Tajbakhsh S. 2018. Unique morphogenetic signatures define mammalian neck muscles and associated connective tissues. *eLife* **7**:eLife7. DOI: <https://doi.org/10.7554/eLife.40179>, PMID: 30451684
- Jimenez MA**, Akerblad P, Sigvardsson M, Rosen ED. 2007. Critical role for Ebf1 and Ebf2 in the adipogenic transcriptional cascade. *Molecular and Cellular Biology* **27**:743–757. DOI: <https://doi.org/10.1128/MCB.01557-06>, PMID: 17060461
- Kameneva P**, Artemov AV, Kastriti ME, Faure L, Olsen TK, Otte J, Erickson A, Semsch B, Andersson ER, Ratz M, Frisén J, Tischler AS, de Krijger RR, Boudierlique T, Akkuratova N, Vorontsova M, Gusev O, Fried K, Sundström E, Mei S, et al. 2021. Single-cell transcriptomics of human embryos identifies multiple sympathoblast lineages with potential implications for neuroblastoma origin. *Nature Genetics* **53**:694–706. DOI: <https://doi.org/10.1038/s41588-021-00818-x>, PMID: 33833454
- Kanisicak O**, Mendez JJ, Yamamoto S, Yamamoto M, Goldhamer DJ. 2009. Progenitors of skeletal muscle satellite cells express the muscle determination gene, MyoD. *Developmental Biology* **332**:131–141. DOI: <https://doi.org/10.1016/j.ydbio.2009.05.554>, PMID: 19464281

- Kardon G**, Harfe BD, Tabin CJ. 2003. A Tcf4-positive mesodermal population provides A prepatter for vertebrate limb muscle patterning. *Developmental Cell* **5**:937–944. DOI: [https://doi.org/10.1016/s1534-5807\(03\)00360-5](https://doi.org/10.1016/s1534-5807(03)00360-5), PMID: 14667415
- Kassar-Duchossoy L**, Gayraud-Morel B, Gomès D, Rocancourt D, Buckingham M, Shinin V, Tajbakhsh S. 2004. Mrf4 determines skeletal muscle identity in Myf5:Myod double-mutant mice. *Nature* **431**:466–471. DOI: <https://doi.org/10.1038/nature02876>, PMID: 15386014
- Knight RD**, Mebus K, Roehl HH. 2008. Mandibular arch muscle identity is regulated by a conserved molecular process during vertebrate development. *Journal of Experimental Zoology. Part B, Molecular and Developmental Evolution* **310**:355–369. DOI: <https://doi.org/10.1002/jez.b.21215>, PMID: 18338789
- Knight JD**, Kothary R. 2011. The myogenic kinome: protein kinases critical to mammalian skeletal myogenesis. *Skeletal Muscle* **1**:29. DOI: <https://doi.org/10.1186/2044-5040-1-29>, PMID: 21902831
- Kuroda S**, Adachi N, Kusakabe R, Kuratani S. 2021. Developmental fates of shark head cavities reveal mesodermal contributions to tendon progenitor cells in extraocular muscles. *Zoological Letters* **7**:e3. DOI: <https://doi.org/10.1186/s40851-021-00170-2>, PMID: 33588955
- La Manno G**, Soldatov R, Zeisel A, Braun E, Hochgerner H, Petukhov V, Lidschreiber K, Kastri ME, Lönnerberg P, Furlan A, Fan J, Borm LE, Liu Z, van Bruggen D, Guo J, He X, Barker R, Sundström E, Castelo-Branco G, Cramer P, et al. 2018. RNA velocity of single cells. *Nature* **560**:494–498. DOI: <https://doi.org/10.1038/s41586-018-0414-6>, PMID: 30089906
- Lagha M**, Brunelli S, Messina G, Cumano A, Kume T, Relaix F, Buckingham ME. 2009. Pax3:Foxc2 reciprocal repression in the somite modulates muscular versus vascular cell fate choice in multipotent progenitors. *Developmental Cell* **17**:892–899. DOI: <https://doi.org/10.1016/j.devcel.2009.10.021>, PMID: 20059958
- Le Douarin N**, Kalcheim C. 1999. Developmental and Cell Biology Series. Cambridge University Press. DOI: <https://doi.org/10.1017/CBO9780511897948>
- Leavitt T**, Hu MS, Borrelli MR, Januszzyk M, Garcia JT, Ransom RC, Mascharak S, desJardins-Park HE, Litzenger UM, Walmsley GG, Marshall CD, Moore AL, Duoto B, Adem S, Foster DS, Salhotra A, Shen AH, Griffin M, Shen EZ, Barnes LA, et al. 2020. Prrx1 Fibroblasts Represent a Pro-fibrotic Lineage in the Mouse Ventral Dermis. *Cell Reports* **33**:108356. DOI: <https://doi.org/10.1016/j.celrep.2020.108356>, PMID: 33176144
- Liao WJ**, Tsao KC, Yang RB. 2016. Electrostatics and N-glycan-mediated membrane tethering of SCUBE1 is critical for promoting bone morphogenetic protein signalling. *The Biochemical Journal* **473**:661–672. DOI: <https://doi.org/10.1042/BJ20151041>, PMID: 26699903
- López-Delgado AC**, Delgado I, Cadenas V, Sánchez-Cabo F, Torres M. 2020. Axial Skeleton Anterior-Posterior Patterning Is Regulated through Feedback Regulation between Meis Transcription Factors and Retinoic Acid. *bioRxiv*. DOI: <https://doi.org/10.1101/2020.03.09.983106>
- Madisen L**, Zwingman TA, Sunkin SM, Oh SW, Zariwala HA, Gu H, Ng LL, Palmiter RD, Hawrylycz MJ, Jones AR, Lein ES, Zeng H. 2010. A robust and high-throughput Cre reporting and characterization system for the whole mouse brain. *Nature Neuroscience* **13**:133–140. DOI: <https://doi.org/10.1038/nn.2467>, PMID: 20023653
- Mathew SJ**, Hansen JM, Merrell AJ, Murphy MM, Lawson JA, Hutcheson DA, Hansen MS, Angus-Hill M, Kardon G. 2011. Connective tissue fibroblasts and Tcf4 regulate myogenesis. *Development (Cambridge, England)* **138**:371–384. DOI: <https://doi.org/10.1242/dev.057463>, PMID: 21177349
- Mayeuf-Louchart A**, Montarras D, Bodin C, Kume T, Vincent SD, Buckingham M. 2016. Endothelial cell specification in the somite is compromised in Pax3-positive progenitors of Foxc1/2 conditional mutants, with loss of forelimb myogenesis. *Development (Cambridge, England)* **143**:872–879. DOI: <https://doi.org/10.1242/dev.128017>, PMID: 26839363
- McDavid A**, Finak G, Gottardo R. 2016. The contribution of cell cycle to heterogeneity in single-cell RNA-seq data. *Nature Biotechnology* **34**:591–593. DOI: <https://doi.org/10.1038/nbt.3498>, PMID: 27281413
- McGinnis CS**, Murrow LM, Gartner ZJ. 2019. DoubletFinder: Doublet Detection in Single-Cell RNA Sequencing Data Using Artificial Nearest Neighbors. *Cell Systems* **8**:329–337. DOI: <https://doi.org/10.1016/j.cels.2019.03.003>, PMID: 30954475
- Muhl L**, Genové G, Leptidis S, Liu J, He L, Mocchi G, Sun Y, Gustafsson S, Buyandelger B, Chivukula IV, Segerstolpe Å, Raschperger E, Hansson EM, Björkegren JLM, Peng X-R, Vanlandewijck M, Lendahl U, Betsholtz C. 2020. Single-cell analysis uncovers fibroblast heterogeneity and criteria for fibroblast and mural cell identification and discrimination. *Nature Communications* **11**:3953. DOI: <https://doi.org/10.1038/s41467-020-17740-1>, PMID: 32769974
- Muzumdar MD**, Tasic B, Miyamichi K, Li L, Luo L. 2007. A global double-fluorescent Cre reporter mouse. *Genesis (New York, N.Y.)* **45**:593–605. DOI: <https://doi.org/10.1002/dvg.20335>, PMID: 17868096
- Nathan E**, Monovich A, Tirosh-Finkel L, Harrelson Z, Rouso T, Rinon A, Harel I, Evans SM, Tzahor E. 2008. The contribution of Islet1-expressing splanchnic mesoderm cells to distinct branchiomeric muscles reveals significant heterogeneity in head muscle development. *Development (Cambridge, England)* **135**:647–657. DOI: <https://doi.org/10.1242/dev.007989>, PMID: 18184728
- Noden DM**, Trainor PA. 2005. Relations and interactions between cranial mesoderm and neural crest populations. *Journal of Anatomy* **207**:575–601. DOI: <https://doi.org/10.1111/j.1469-7580.2005.00473.x>, PMID: 16313393
- Noden DM**, Epstein ML. 2010. Embryonic origins of avian and mammalian laryngeal musculoskeletal structures. *The FASEB Journal* **24**:172. DOI: [https://doi.org/10.1096/fasebj.24.1\\_supplement.172.1](https://doi.org/10.1096/fasebj.24.1_supplement.172.1)
- Noizet M**, Lagoutte E, Gratigny M, Bouschbacher M, Lazareth I, Roest Crollius H, Darzacq X, Dugast-Darzacq C. 2016. Master regulators in primary skin fibroblast fate reprogramming in a human ex vivo model of chronic



- wounds. *Wound Repair and Regeneration* **24**:247–262. DOI: <https://doi.org/10.1111/wrr.12392>, PMID: 26663515
- Olson LE**, Soriano P. 2009. Increased PDGFR $\alpha$  activation disrupts connective tissue development and drives systemic fibrosis. *Developmental Cell* **16**:303–313. DOI: <https://doi.org/10.1016/j.devcel.2008.12.003>, PMID: 19217431
- Prummel KD**, Nieuwenhuize S, Mosimann C. 2020. The lateral plate mesoderm. *Development (Cambridge, England)* **147**:dev175059. DOI: <https://doi.org/10.1242/dev.175059>, PMID: 32561665
- Puré E**, Blomberg R. 2018. Pro-tumorigenic roles of fibroblast activation protein in cancer: back to the basics. *Oncogene* **37**:4343–4357. DOI: <https://doi.org/10.1038/s41388-018-0275-3>, PMID: 29720723
- Qiu C**, Cao J, Li T, Srivatsan S, Huang X, Calderon D, Noble WS, Disteche CM, Spielmann M, Moens CB, Trapnell C, Shendure J. 2021. Systematic Reconstruction of the Cellular Trajectories of Mammalian Embryogenesis. *Developmental Biology* **1**:447626. DOI: <https://doi.org/10.1101/2021.06.08.447626>
- Sacchetti B**, Funari A, Remoli C, Giannicola G, Kogler G, Liedtke S, Cossu G, Serafini M, Sampaolesi M, Tagliafico E, Tenedini E, Saggio I, Robey PG, Riminucci M, Bianco P. 2016. No Identical “Mesenchymal Stem Cells” at Different Times and Sites: Human Committed Progenitors of Distinct Origin and Differentiation Potential Are Incorporated as Adventitial Cells in Microvessels. *Stem Cell Reports* **6**:897–913. DOI: <https://doi.org/10.1016/j.stemcr.2016.05.011>, PMID: 27304917
- Saga Y**, Miyagawa-Tomita S, Takagi A, Kitajima S, Miyazaki J i., Inoue T. 1999. MesP1 is expressed in the heart precursor cells and required for the formation of a single heart tube. *Development (Cambridge, England)* **126**:3437–3447. DOI: <https://doi.org/10.1242/dev.126.15.3437>, PMID: 10393122
- Sambasivan R**, Gayraud-Morel B, Dumas G, Cimper C, Paisant S, Kelly RG, Kelly R, Tajbakhsh S. 2009. Distinct regulatory cascades govern extraocular and pharyngeal arch muscle progenitor cell fates. *Developmental Cell* **16**:810–821. DOI: <https://doi.org/10.1016/j.devcel.2009.05.008>, PMID: 19531352
- Sebo ZL**, Jeffery E, Holtrup B, Rodeheffer MS. 2018. A mesodermal fate map for adipose tissue. *Development (Cambridge, England)* **145**:dev166801. DOI: <https://doi.org/10.1242/dev.166801>, PMID: 30045918
- Sefton EM**, Kardon G. 2019. Connecting muscle development, birth defects, and evolution: An essential role for muscle connective tissue. *Current Topics in Developmental Biology* **132**:137–176. DOI: <https://doi.org/10.1016/bs.ctdb.2018.12.004>, PMID: 30797508
- Shao X**, Wei X. 2018. FOXP1 enhances fibrosis via activating Wnt/ $\beta$ -catenin signaling pathway in endometriosis. *American Journal of Translational Research* **10**:3610–3618 PMID: 30662612.,
- Spörle R**. 2001. Epaxial-adaxial-hypaxial regionalisation of the vertebrate somite: evidence for a somitic organiser and a mirror-image duplication. *Development Genes and Evolution* **211**:198–217. DOI: <https://doi.org/10.1007/s004270100139>, PMID: 11455436
- Stuelsatz P**, Shearer A, Yablonka-Reuveni Z. 2014. Ancestral Myf5 gene activity in periocular connective tissue identifies a subset of fibro/adipogenic progenitors but does not connote a myogenic origin. *Developmental Biology* **385**:366–379. DOI: <https://doi.org/10.1016/j.ydbio.2013.08.010>, PMID: 23969310
- Swedlund B**, Lescroart F. 2020. Cardiopharyngeal Progenitor Specification: Multiple Roads to the Heart and Head Muscles. *Cold Spring Harbor Perspectives in Biology* **12**:a036731. DOI: <https://doi.org/10.1101/cshperspect.a036731>, PMID: 31818856
- Tajbakhsh S**, Rocancourt D, Buckingham M. 1996. Muscle progenitor cells failing to respond to positional cues adopt non-myogenic fates in myf-5 null mice. *Nature* **384**:266–270. DOI: <https://doi.org/10.1038/384266a0>, PMID: 8918877
- Tallquist MD**, Weismann KE, Hellstrom M, Soriano P. 2000. Early myotome specification regulates PDGFA expression and axial skeleton development. *Development* **127**:5059–5070. DOI: <https://doi.org/10.1242/dev.127.23.5059>
- Tapscott SJ**. 2005. The circuitry of a master switch: MyoD and the regulation of skeletal muscle gene transcription. *Development (Cambridge, England)* **132**:2685–2695. DOI: <https://doi.org/10.1242/dev.01874>, PMID: 15930108
- Truong AH**, Ben-David Y. 2000. The role of Fli-1 in normal cell function and malignant transformation. *Oncogene* **19**:6482–6489. DOI: <https://doi.org/10.1038/sj.onc.1204042>, PMID: 11175364
- Tzahor E**, Kempf H, Mootosamy RC, Poon AC, Abzhanov A, Tabin CJ, Dietrich S, Lassar AB. 2003. Antagonists of Wnt and BMP signaling promote the formation of vertebrate head muscle. *Genes & Development* **17**:3087–3099. DOI: <https://doi.org/10.1101/gad.1154103>, PMID: 14701876
- van de Moosdijk AAA**, van de Grift YBC, de Man SMA, Zeeman AL, van Amerongen R. 2020. A novel Axin2 knock-in mouse model for visualization and lineage tracing of WNT/CTNNB1 responsive cells. *Genesis (New York, N.Y)* **58**:e23387. DOI: <https://doi.org/10.1002/dvg.23387>, PMID: 32643876
- Van de Sande B**, Flerin C, Davie K, De Waegeneer M, Hulselmans G, Aibar S, Seurinck R, Saelens W, Cannoodt R, Rouchon Q, Verbeiren T, De Maeyer D, Reumers J, Saeys Y, Aerts S. 2020. A scalable SCENIC workflow for single-cell gene regulatory network analysis. *Nature Protocols* **15**:2247–2276. DOI: <https://doi.org/10.1038/s41596-020-0336-2>, PMID: 32561888
- Vinagre T**, Moncaut N, Carapuço M, Nóvoa A, Bom J, Mallo M. 2010. Evidence for a myotomal Hox/Myf cascade governing nonautonomous control of rib specification within global vertebral domains. *Developmental Cell* **18**:655–661. DOI: <https://doi.org/10.1016/j.devcel.2010.02.011>, PMID: 20412779
- Wang W**, Niu X, Stuart T, Jullian E, Mauck WM, Kelly RG, Satija R, Christiaen L. 2019. A single-cell transcriptional roadmap for cardiopharyngeal fate diversification. *Nature Cell Biology* **21**:674–686. DOI: <https://doi.org/10.1038/s41556-019-0336-z>, PMID: 31160712



- Wang L**, Tang Q, Xu J, Li H, Yang T, Li L, Machon O, Hu T, Chen Y. 2020. The transcriptional regulator MEIS2 sets up the ground state for palatal osteogenesis in mice. *The Journal of Biological Chemistry* **295**:5449–5460. DOI: <https://doi.org/10.1074/jbc.RA120.012684>, PMID: 32169905
- Whitesell TR**, Chrystal PW, Ryu JRR, Munsie N, Grosse A, French CR, Workentine ML, Li R, Zhu LJ, Waskiewicz A, Lehmann OJ, Lawson ND, Childs SJ. 2019. foxc1 is required for embryonic head vascular smooth muscle differentiation in zebrafish. *Developmental Biology* **453**:34–47. DOI: <https://doi.org/10.1016/j.ydbio.2019.06.005>, PMID: 31199900
- Wood WM**, Otis C, Etemad S, Goldhamer DJ. 2020. Development and patterning of rib primordia are dependent on associated musculature. *Developmental Biology* **468**:133–145. DOI: <https://doi.org/10.1016/j.ydbio.2020.07.015>, PMID: 32768399
- Xu P**, Yu HV, Tseng KC, Flath M, Fabian P, Segil N, Crump JG. 2021. Foxc1 establishes enhancer accessibility for craniofacial cartilage differentiation. *eLife* **10**:63595. DOI: <https://doi.org/10.7554/eLife.63595>
- Yamamoto-Shiraishi Y**, Kuroiwa A. 2013. Wnt and BMP signaling cooperate with Hox in the control of Six2 expression in limb tendon precursor. *Developmental Biology* **377**:363–374. DOI: <https://doi.org/10.1016/j.ydbio.2013.02.023>, PMID: 23499659
- Zacharias AL**, Lewandoski M, Rudnicki MA, Gage PJ. 2011. Pitx2 is an upstream activator of extraocular myogenesis and survival. *Developmental Biology* **349**:395–405. DOI: <https://doi.org/10.1016/j.ydbio.2010.10.028>, PMID: 21035439